APPLIED SCIENCES AND ENGINEERING

Single-cell analysis of the decidua unveils the mechanism of anti-inflammatory exosomes for chorioamnionitis in nonhuman primates

Seung Hyun Jang[1]†, Hojun Choi[2]†‡, Eun Mi Lee[3,4]†, Seung-Bin Yoon[5], Hye-Jung Kim[2,6], Cheolhyoung Park[2], Jae Kyung Won[7], Seung Han Shin[8], Ji-Su Kim[5]*, Chan-Wook Park[3,4]*, Heon Yung Gee[1]*, Chulhee Choi[2]*

The effectiveness of exosomes engineered to carry a dominantly active variant of inhibitor α of nuclear factor κB (NF-κB) (IκBα), super-repressor IκB (srIκB), that inhibits the expression of NF-κB in various animal models of inflammatory diseases has been demonstrated. In this study, we used a lipopolysaccharide (LPS)–induced chorioamnionitis model in pregnant nonhuman primates to explore the therapeutic potential and mode of action of srIκB-loaded exosomes (Exo-srIκBs). Intraamniotic injection of LPS induced infiltration of BCL2A1-positive neutrophils and CD68-positive macrophages in the extraplacental membranes, causing fetal lung injury. Conversely, administration of Exo-srIκB via intraamniotic and intravenous routes (6.9×10^{10} and 4×10^{11} particle numbers, respectively) ameliorated these effects. Single-cell RNA sequencing of the decidua and bulk RNA sequencing of the choriodecidua highlighted that Exo-srIκB treatment mitigated LPS-induced inflammatory pathways, particularly in macrophages, leading to a cascade effect on neutrophils through NF-κB signaling inhibition. These findings underscore the potential of Exo-srIκB as a therapeutic strategy for chorioamnionitis.

INTRODUCTION

Chorioamnionitis, also known as intrauterine inflammation, is an inflammation of the fetal membranes (amnion and chorion), mostly owing to ascending bacterial infections, and is a notable cause of preterm birth (PTB) and various neonatal and maternal morbidities (*1*–*6*). Although chorioamnionitis is only seen in ~4% of full-term deliveries, its incidence rises considerably in PTB and cases of premature membrane rupture, accounting for ~40% of preterm labor (*1*, *7*). Chorioamnionitis involves a complex immune response, where ascending infection triggers an inflammatory cascade characterized by the infiltration of neutrophils and release of inflammatory cytokines at the maternal-fetal interface, leading to adverse fetal and neonatal outcomes (*2*). Notably, we previously demonstrated that the progression of intrauterine inflammation in multiple placental compartments [i.e., extraplacental membranes (EPMs), umbilical cord, and chorionic plate] significantly correlates with intraamniotic and fetal inflammatory responses, as well as neonatal morbidities (i.e., early-onset neonatal sepsis) (*8*–*12*). Therefore, controlling intrauterine inflammation, such as chorioamnionitis, may serve as an effective strategy for improving neonatal outcomes.

Current antibiotic treatments, while standard, fail to adequately prevent morbidities associated with chorioamnionitis, as they do not address the residual inflammation that causes fetal and maternal injury (*13*–*17*). Furthermore, numerous studies have restricted the administration of commonly used anti-inflammatory drugs, such as nonsteroidal anti-inflammatory drugs (NSAIDs), to a limited period (typically 24 to 48 hours), as therapeutic doses of NSAIDs, such as indomethacin, may induce oligohydramnios, disrupt the normal development of the kidneys, and reduce renal perfusion and ultrafiltration of the fetal kidneys, possibly leading to acute kidney injury in newborns (*18*, *19*). These issues underscore the need for innovative therapeutic strategies for suppressing inflammation in pregnant women at the risk of developing PTB associated with chorioamnionitis. Nuclear factor κB (NF-κB) serves as a pivotal transcription factor (TF) in chorioamnionitis pathophysiology that initiates a robust inflammatory response by up-regulating proinflammatory cytokines and mediators, while also recruiting and activating neutrophils at the maternal-fetal interface (*2*, *20*, *21*). Furthermore, the dysregulation of NF-κB signaling has been linked to adverse neonatal outcomes, suggesting its potential as a therapeutic target for modulating intrauterine inflammation (*13*). While NF-κB inhibitors such as *N*-acetylcysteine (*22*–*26*), sulfasalazine (*27*), cytokine-suppressive anti-inflammatory drugs (*28*, *29*), selective kinase complex inhibitors, and NSAIDs (*17*, *30*, *31*) have demonstrated potential in reducing inflammation, their clinical efficacy against chorioamnionitis and in improving fetal outcomes remains limited; this is partly attributed to their limited bioavailability, challenges in drug delivery, placental transfer issues, limited efficacy in mitigating fetal inflammation, and potential teratogenic effects, which restrict their clinical advancement.

In this study, we investigated the therapeutic potential and mode of action of engineered anti-inflammatory exosomes in a lipopolysaccharide (LPS)–induced nonhuman primate (NHP) model of chorioamnionitis using single-cell RNA sequencing (scRNA-seq) of the decidua and bulk RNA-seq of the choriodecidua of EPMs (Fig. 1A).

[1]Department of Pharmacology, Graduate School of Medical Science, Brain Korea 21 Project, Yonsei University College of Medicine, Seoul, Korea. [2]ILIAS Biologics Inc., Daejeon, Korea. [3]Department of Obstetrics and Gynecology, Seoul National University Hospital, Seoul National University College of Medicine, Seoul, Korea. [4]Institute of Reproductive Medicine and Population, Medical Research Center, Seoul National University, Seoul, 03087, Korea. [5]Primate Resources Center (PRC), Korea Research Institute of Bioscience and Biotechnology (KRIBB), Jeongeup-si, Jeollabuk-do, Korea. [6]Korea Institute of Ceramic Engineering and Technology, Cheongju, 28160, Korea. [7]Department of Pathology, Seoul National University Hospital, Seoul National University College of Medicine, Seoul, Korea. [8]Department of Pediatrics, Seoul National University Hospital, Seoul National University College of Medicine, Seoul, Korea.
*Corresponding author. Email: cchoi@iliasbio.com (C.C.); hygee@yuhs.ac (H.Y.G.); cspark99@snu.ac.kr (C.-W.P.); kimjs@kribb.re.kr (J.-S.K.)
†These authors contributed equally to this work.
‡Present address: Department of Biochemistry and Institute for Protein Design, University of Washington, Seattle, WA, USA.

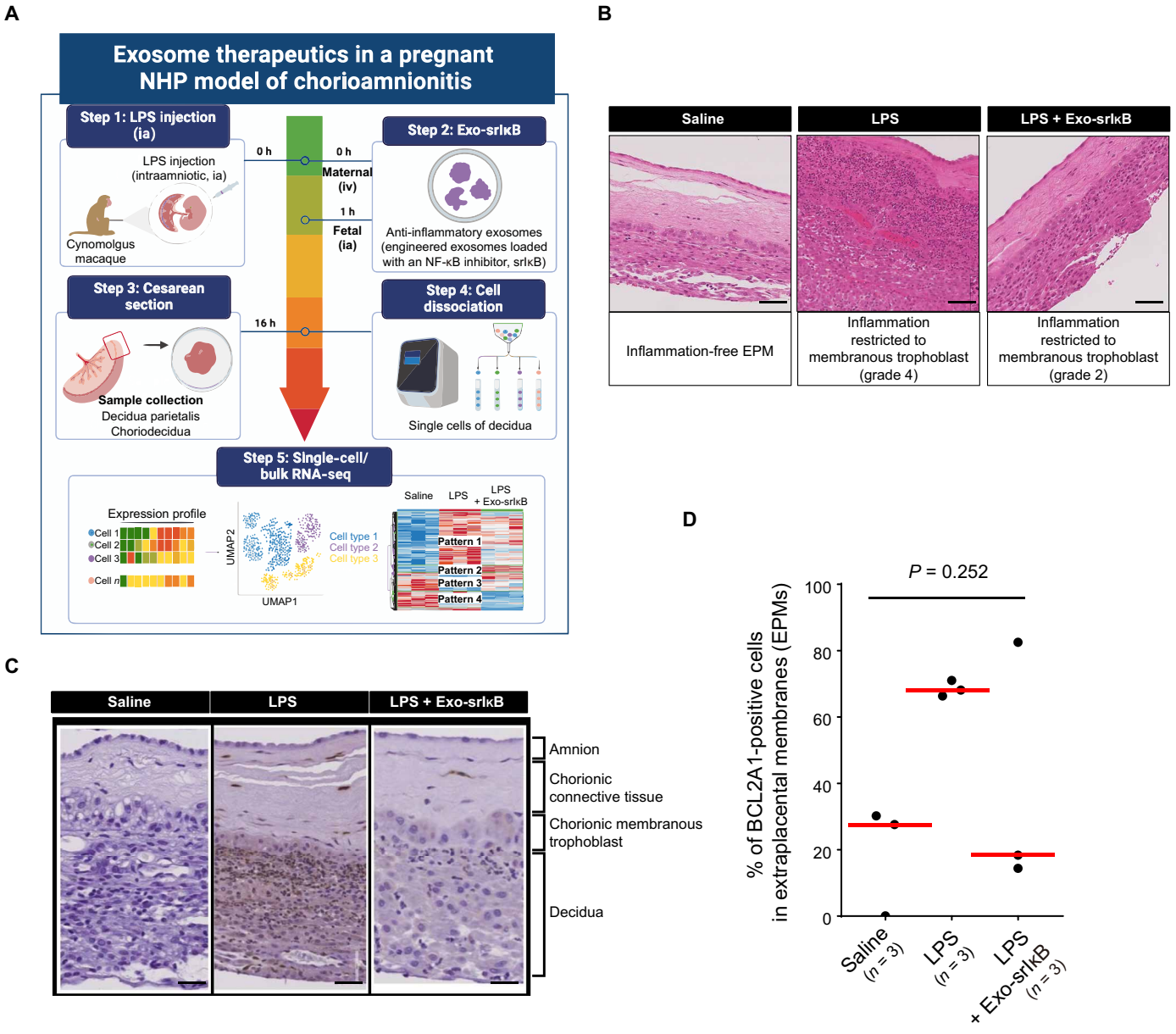

Fig. 1. Study design and histopathological assessment of cynomolgus macaque choriodecidua postintervention. (**A**) Overview of experimental design. Cynomolgus macaques received intraamniotic (ia) LPS injections at 0 hours (h) to induce chorioamnionitis, followed by intravenous (iv) and intraamniotic administration of Exo-srIκB at 0 and 1 hour post–LPS injection, respectively. Decidua tissue and choriodecidua of EPMs were collected for downstream analyses. UMAP, uniform manifold approximation and projection. (**B**) Representative images of EPM from three treatment groups: saline, inflammation-free EPM; LPS, inflammation restricted to membranous trophoblast, grade 4; LPS + Exo-srIκB, inflammation restricted to membranous trophoblast, grade 2. Scale bars, 100 μm. (**C**) Representative immunohistochemical images of BCL2A1 staining in EPM from the three treatment groups. Scale bars, 50 μm. (**D**) Digital image analysis using QuPath to determine the percentage of BCL2A1-positive cells in EPM from the three treatment groups. Data are presented as median with individual values ($n = 3$ biological replicates per group). Kruskal-Wallis test was performed to determine statistical significance among the three groups, with the calculated *P* value indicated in the plots.

Using the EXPLOR technique (*32*), we engineered exosomes encapsulating a robust NF-κB inhibitor known as super-repressor inhibitor of NF-κB (IκB) (srIκB). This mutant IκBα variant is resistant to phosphorylation-triggered degradation, thereby impeding NF-κB nuclear translocation and subsequent proinflammatory gene transcription, even under inflammatory stimuli (*33*, *34*). We have previously shown that exosomes loaded with srIκB (Exo-srIκBs) are effective in mitigating inflammation in various murine models of inflammatory diseases such as inflammation-induced PTB (*35*), sepsis (*36*), kidney ischemia-reperfusion injury (*37*), chronic post-ischemia pain (*38*), rheumatoid arthritis (*39*), and age-related neuroinflammation (*40*). In this study, we aimed to explore whether intraamniotic and intravenous administration of Exo-srIκB can relieve inflammatory response in the EPM of an LPS-induced chorioamnionitis model in NHP. The strategy of concurrent intravenous and intraamniotic administration of exosomes in this study was

predicated on the basis of the ability of exosomes to cross the placental barrier, thus maximizing the therapeutic effect in both maternal (i.e., decidua) and fetal (i.e., membranous chorion and amniotic fluid) compartments. Notably, we observed a decreasing trend in neutrophil infiltration and the expression of B-cell lymphoma 2-related protein A1 (BCL2A1), a marker of the presence of inflammatory neutrophils in the choriodecidua (*20*), and $CD68^+$ macrophages, with significant changes in their composition, in the EPM following Exo-srIκB administration. scRNA-seq analysis of decidua tissues highlighted macrophages and neutrophils as primary target cells to the treatment, which exhibited significant attenuation of LPS-induced surge in inflammatory M1 macrophages and neutrophils, alongside a downshift in inflammatory response–related gene expressions. Subsequent analyses underscored a cascading effect whereby reducing macrophage-driven inflammation sequentially diminished neutrophilic responses. Bulk RNA-seq data further corroborated the anti-inflammatory effect of Exo-srIκB on the choriodecidua of the EPM. Moreover, we observed a significant alleviation in LPS-induced fetal lung injury following Exo-srIκB treatment, suggesting the potential of Exo-srIκB treatment for improving neonatal respiratory comorbidities associated with chorioamnionitis. To the best of our knowledge, this investigation is the first to evaluate the therapeutic efficacy and mechanistic action of engineered exosomes in an NHP chorioamnionitis model, which is a critical step toward clinical translation.

RESULTS

Histopathological assessment of chorioamnionitis in the EPMs and single-cell transcriptomic profiling of cynomolgus macaque decidua

To induce intrauterine inflammation, we intraamniotically injected cynomolgus macaques at a gestational age of 130 to 133 days with 1 mg of LPS. The LPS dosage and administration route were determined on the basis of previously reported chorioamnionitis models in NHP (*20*, *41*, *42*). This was followed by the administration of Exo-srIκB via intravenous route [4×10^{11} particle numbers (pn)] and intraamniotic injection (6.9×10^{10} pn) at 0 and 1 hour post–LPS administration, respectively (Fig. 1A). Pathological examination of the EPM post–LPS treatment demonstrated a marked infiltration of neutrophils (grade 4), with the inflammation restricted to the membranous trophoblast, in contrast to that in the saline-injected group. Contrastingly, Exo-srIκB treatment following LPS stimulation substantially reduced the infiltration of neutrophils (grade 2), with the inflammation confined to the membranous trophoblast (Fig. 1B). Notably, we found that the number of BCL2A1-positive cells, a surrogate marker of neutrophil infiltration and survival in the EPM (*20*), increased in the LPS-injected group compared with that in the saline-injected group; however, this difference did not reach statistical significance due to the small sample size. Conversely, Exo-srIκB administration following LPS stimulation tended to reduce the number of BCL2A1-positive cells (Fig. 1, C and D). Immunofluorescent staining for neutrophils (neutrophil $elastase^+$), macrophages ($CD68^+$), and BCL2A1 corroborated the findings presented in Fig. 1 (B to D) as follows: (i) Intraamniotic LPS injection induced the infiltration of BCL2A1-expressing neutrophils (neutrophil $elastase^+$ $BCL2A1^+$), primarily localized in the membranous trophoblast of the chorion. Subsequent to Exo-srIκB administration, the infiltrating neutrophils were markedly diminished (Fig. 2A). (ii) Although intraamniotic LPS injection increased the infiltration of $CD68^+$ macrophages, their recruitment was relatively smaller than that of neutrophils, and their numbers similarly decreased following Exo-srIκB administration (Fig. 2B). (iii) Notably, in the EPM, BCL2A1 was primarily expressed by neutrophils after LPS stimulation, as evidenced by the findings that most polymorphonuclear cells exhibiting neutrophil morphology coexpressed neutrophil elastase and BCL2A1 (fig. S1).

In addition, to investigate monocyte/macrophage (MoMA) composition in the EPM, we analyzed the $CD45^+$ $CD11b^+$ decidua cells via flow cytometry using anti-CD14 and anti-CD16 antibodies, which identified three monocyte subsets: classical ($CD14^+$ $CD16^{dim}$), intermediate ($CD14^+$ $CD16^+$), and nonclassical ($CD14^{dim}$ $CD16^+$) monocytes (fig. S2A). Classical monocytes are associated with phagocytosis, innate immune response, and migration into inflamed tissues (*43*, *44*), while nonclassical monocytes are related to wound healing and exert an anti-inflammatory role (*45*). Notably, the MoMA composition differed significantly across the three conditions (fig. S2B). We observed an increasing trend in the proportion of classical monocytes and a decreasing trend in nonclassical monocytes in the LPS-stimulated group compared to the saline-injected group. By contrast, following Exo-srIκB administration, classical monocytes tended to decrease, while a partial recovery in the proportion of nonclassical monocytes was detected compared to the LPS-injected group. Moreover, Exo-srIκB treatment reduced the expression of NF-κB–p65, a marker of the activation of NF-κB signaling (*46*), compared with that in the LPS-injected group; however, this reduction did not reach statistical significance due to the small sample size. In the LPS-injected group, NF-κB–p65 expression showed an increasing trend compared to the saline-injected group (fig. S3).

To obtain a comprehensive molecular landscape of the various cells in the decidua, we conducted scRNA-seq of cynomolgus macaque decidua tissues. Samples were collected from six cynomolgus macaques that were separately injected with saline, LPS, and LPS + Exo-srIκB ($n = 2$ each). After assessing quality control metrics and filtering out the low-quality cells (fig. S4, A to D), we analyzed 57,848 cells. Among these, 22,102 cells belonged to the saline-injected group, 16,514 cells belonged to the LPS-injected group, and 19,232 cells belonged to the LPS + Exo-srIκB–injected group. This analysis led to the identification of 18 distinct cell types (Fig. 3A), which encompass major cell lineages, such as epithelial cells, fibroblasts, vascular/lymphatic endothelial cells, neutrophils, macrophages, B-cells, $CD8^+$ or $CD4^+$ T cells, and natural killer (NK) cells; these cells were distinguished on the basis of their expression of established marker genes (Fig. 3B). The composition of cell types within the decidua markedly changed across the three treatment groups. Following LPS stimulation, we observed a prominent increase in the number of neutrophils and macrophages, specifically M1-like macrophages. However, Exo-srIκB treatment following LPS stimulation led to a considerable reduction in the number of neutrophils and macrophages (Fig. 3C). These results, in conjunction with the observations from the histopathologic assessment of the EPM (see Figs. 1 and 2), suggested that our model accurately recapitulated the characteristics of infection-induced preterm chorioamnionitis, which is characterized by the robust infiltration of innate immune cells such as neutrophils and macrophages (*47*–*50*). Furthermore, Exo-srIκB therapy showed efficacy in reducing the infiltration of these cells into the decidua.

Alterations in the molecular profile of immune cells in the decidua

To examine the effect of Exo-srIκB treatment on the expression patterns of various immune cells in the decidua, we first evaluated the

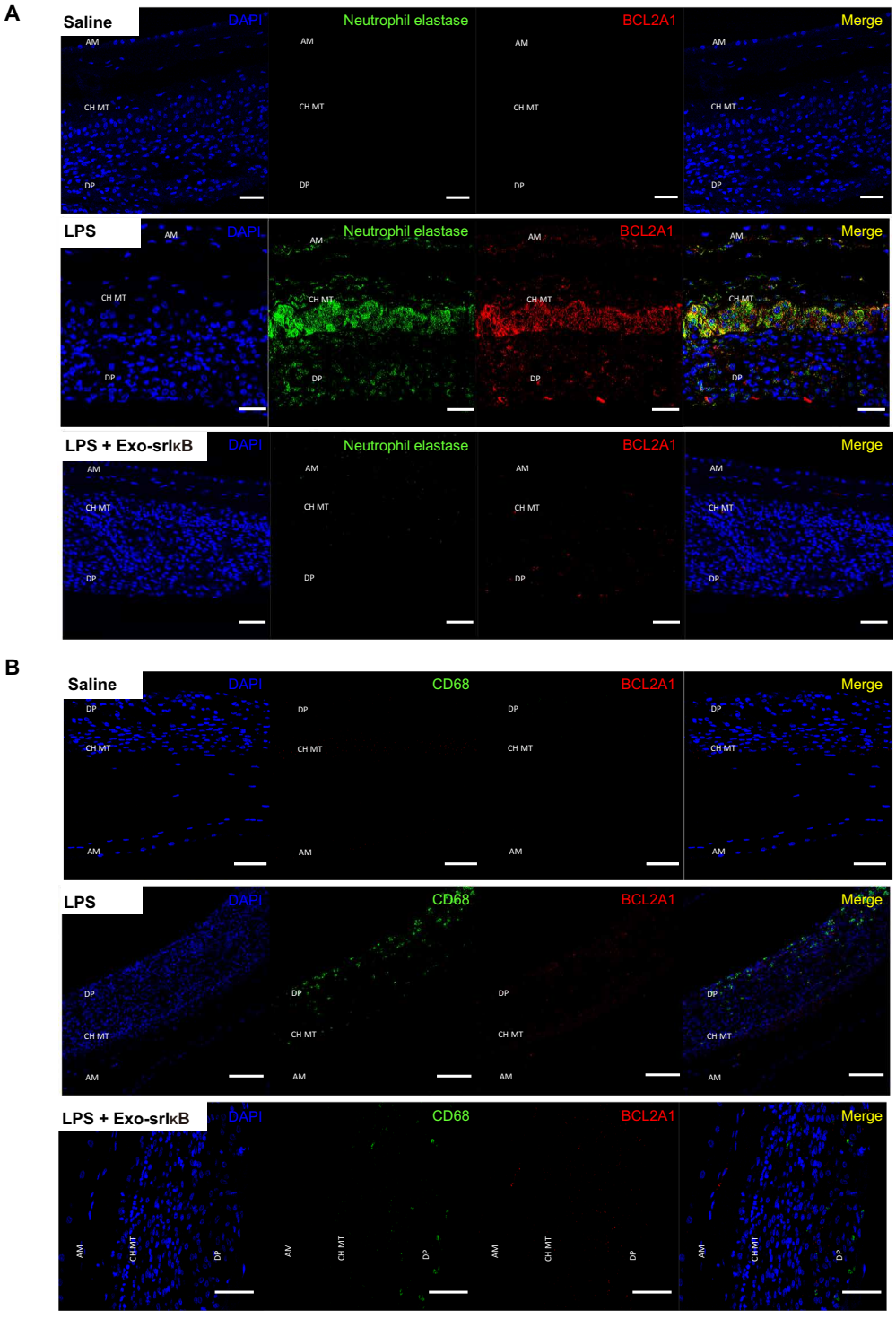

Fig. 2. Immunofluorescent staining of BCL2A1 with neutrophils and macrophages in the EPMs. (**A**) Representative images of the EPM from the three treatment groups stained with 4′,6-diamidino-2-phenylindole (DAPI; blue), neutrophil elastase as a marker for neutrophils (green), and BCL2A1 (red). Scale bars, 50 μm (saline and LPS groups) and 100 μm (LPS + Exo-srIκB group). (**B**) Representative images of the EPM from the three treatment groups stained with DAPI (blue), CD68 as a marker for macrophages (green), and BCL2A1 (red). Scale bars, 50 μm (saline and LPS + Exo-srIκB groups) and 100 μm (LPS group). AM, amnion; CH MT, chorion membranous trophoblast; DP, decidua parietalis.

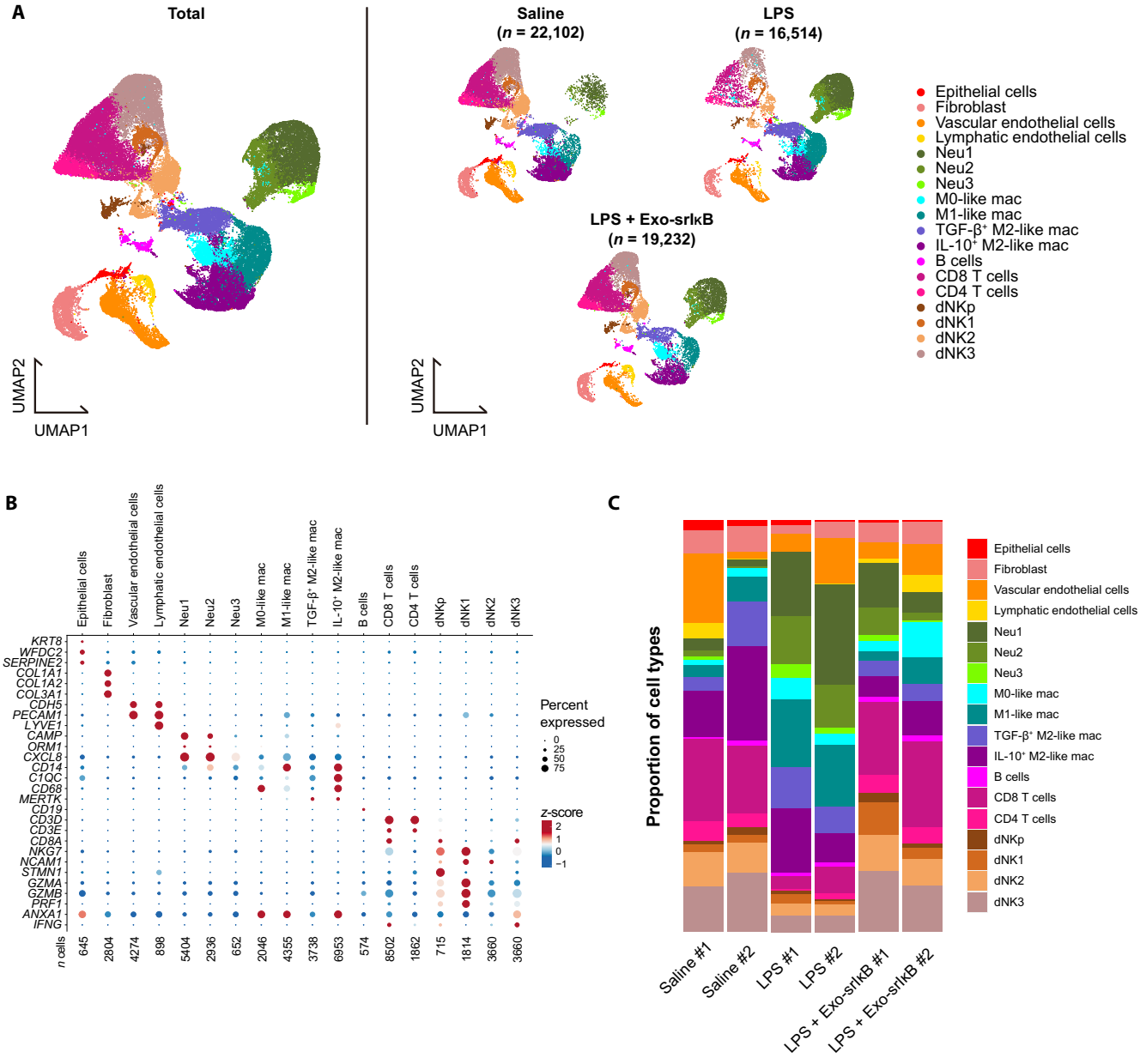

Fig. 3. scRNA-seq of cynomolgus macaque decidua. (**A**) Uniform manifold approximation and projection of scRNA-seq data, consisting of 57,848 cells (saline, 22,102 cells; LPS, 16,514 cells; LPS + Exo-srIκB, 19,232 cells). Neu, neutrophils; mac, macrophages; dNK, decidua NK cells; p, proliferative. (**B**) Dot plot illustrating marker genes for the identified cell subtypes. Dot size and color represent the percentage of cells expressing specific marker genes within each cell type and *z*-score of normalized expression values, respectively. The number of identified cells for each subtype is presented beneath the dot plot. (**C**) Bar plot showing the proportion of cell types in each individual animal.

number of significantly differentially expressed genes (DEGs) among the three treatment groups. After LPS stimulation, we noticed a substantially greater number of DEGs in neutrophils and macrophages compared with other types of immune cells such as B, T, and NK cells, in contrast to that in the saline-injected group. However, when Exo-srIκB was administered following LPS stimulation, macrophages had a much greater degree of differential expression than other immune cell types, in contrast to that in the group injected with LPS alone (Fig. 4A). Consistent with the number of DEGs identified in each cell type, Q-Q plots revealed that LPS stimulation predominantly affected neutrophils and macrophages. By contrast, Exo-srIκB + LPS administration had a more pronounced effect on macrophages, especially M0-like macrophages compared with LPS stimulation alone (fig. S5, A and B). These findings suggested that Exo-srIκB primarily modulates macrophages.

Next, we evaluated the alterations in the expression profile and molecular signature of neutrophils and macrophages, which exhibited a greater number of DEGs across the three treatment groups. Initially, to determine the characteristics of the three subtypes of neutrophils, we compared the signatures of neutrophil activation

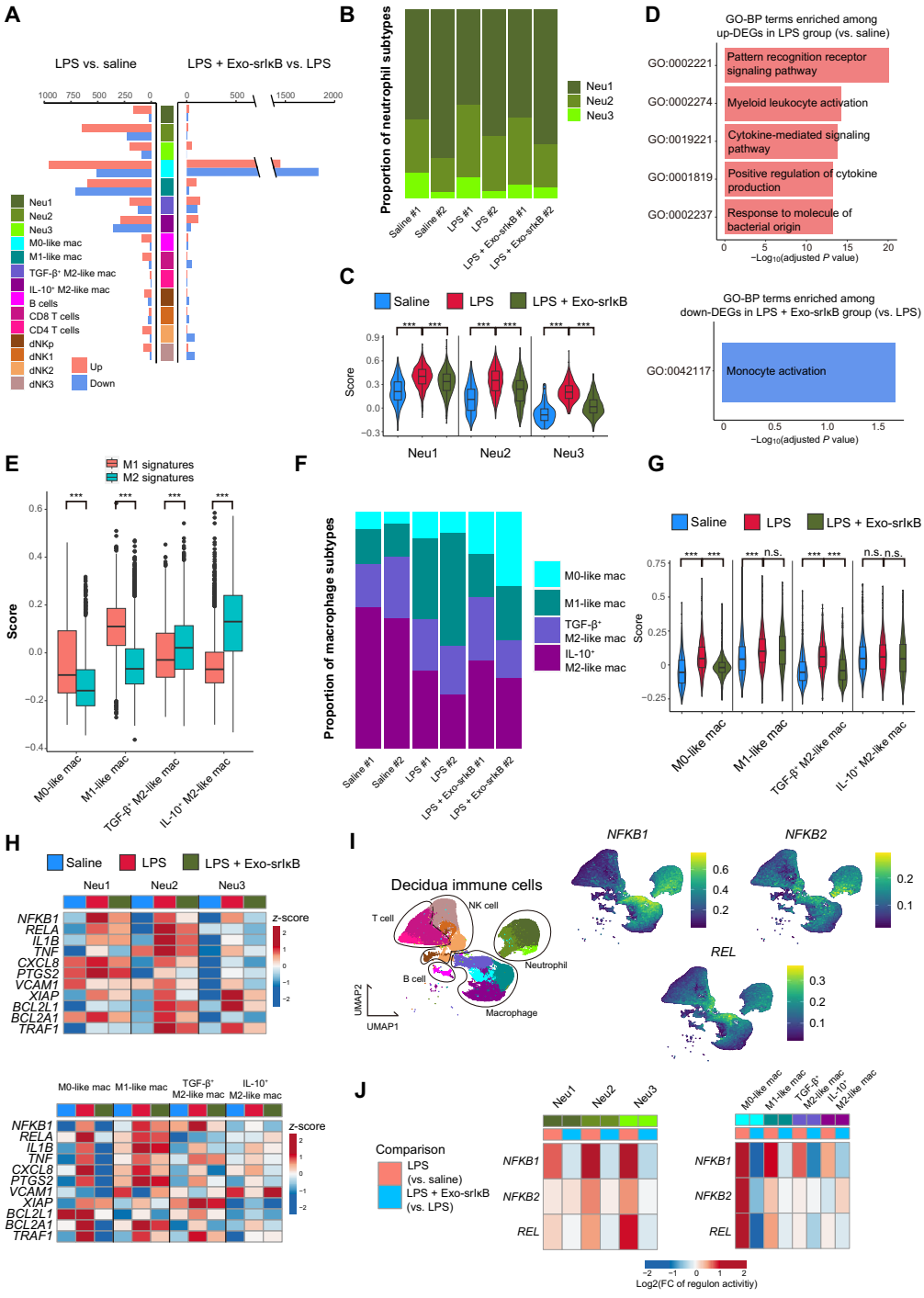

Fig. 4. Changes in the composition and molecular signatures of immune cells among the three groups. (**A**) Number of significantly DEGs [Benjamini-Hochberg (BH)–adjusted $P < 0.05$] in each cell type: LPS versus saline-injected groups (left) and LPS + Exo-srIκB versus LPS-injected groups (right). (**B**) Proportion of neutrophil subtypes in each individual animal. (**C**) Violin plots depicting neutrophil activation scores among the three groups. One-way analysis of variance (ANOVA) with Bonferroni correction for multiple comparisons was performed. n.s., not significant. $***P \leq 0.001$. (**D**) Top 5 (or fewer) gene ontology (GO) biological process (BP) terms with Benjamini-Hochberg–adjusted $P < 0.05$ enriched among significant DEGs in neutrophils between the two compared groups. (**E**) Box plots presenting M1 and M2 signature scores in each macrophage subtype. Paired *t* tests were performed between the two signature scores. $***P \leq 0.001$. (**F**) The proportion of macrophage subtypes in each individual animal. (**G**) Violin plots showing macrophage classical activation scores among the three groups. One-way ANOVA with Bonferroni correction for multiple comparisons was performed. $***P \leq 0.001$. (**H**) Heatmap presenting the *z*-scored, normalized expression levels of representative target genes from canonical NF-κB signaling in neutrophils and macrophages among the three groups. (**I**) Regulon activities of the identified NF-κB family TFs (*NFKB1*, *NFKB2*, and *REL*) projected onto the UMAP plot. Only decidua immune cells are shown. (**J**) Heatmap displaying the $\log_2$ fold changes (FCs) of average regulon activities in neutrophils and macrophages, comparing the LPS-injected with the saline-injected (light coral) group and the LPS + Exo-srIκB–injected with the LPS-injected (sky blue) group.

and maturation and found that the neutrophil 1 (Neu1) subtype displayed significantly higher scores for both activation and maturation compared with those in the other two subtypes (fig. S6, A and B). The composition of the three subtypes of neutrophils remained largely unchanged and consistent across different conditions (Fig. 4B). However, the neutrophil activation score was significantly increased in the LPS-injected group compared with that in the saline-injected group. Conversely, in the LPS + Exo-srIκB group, the degree of neutrophil activation was significantly decreased compared with that in the group treated with LPS alone, across all subtypes of neutrophils (Fig. 4C). In addition, gene ontology (GO) biological process enrichment analysis showed that, compared with the saline group, the up-regulated DEGs in neutrophils in the LPS-injected group were associated with biological processes such as pattern recognition receptor signaling, myeloid leukocyte activation, and cytokine-mediated signaling. This finding suggested the activation of neutrophils and the innate immune system of the decidua. Compared with the LPS-injected group, in the LPS + Exo-srIκB group, the down-regulated DEGs of neutrophils were related to monocyte activation, suggesting the decreased activation of neutrophils following Exo-srIκB treatment (Fig. 4D).

Regarding macrophages, we initially assessed the polarization of each macrophage subtype and distinguished one M0-like, one M1-like, and two M2-like macrophages by comparing the M1 and M2 signature scores within each subtype and examining the expression levels of decidua M1- or M2-related genes (Fig. 4E and fig. S7, A and B) (*51*, *52*). The expression of marker genes associated with M1-like macrophages was enriched in processes related to classical activation of macrophages, such as leukocyte migration, activation, and phagocytosis. In addition, the inflammatory response and activation score of myeloid leukocytes were higher in M1-like macrophages. The interleukin-10–positive (IL-10$^+$) M2-like macrophage showed enrichment of marker genes associated with antigen processing, presentation, and viral process, while demonstrating a higher score for tissue regeneration (fig. S7, C and D). Unlike neutrophils, the composition of macrophages underwent marked changes under different conditions. Specifically, we detected a higher percentage of M1-like macrophages in the LPS-treated group than in the saline-treated group, whereas the Exo-srIκB–treated group showed a considerable decrease in the number of M1-like macrophages and partial recovery of M2-like macrophages compared with those in the LPS-treated group (Fig. 4F). In addition to changes in the proportion of subtypes, the macrophage classical activation score was increased following LPS stimulation in M0-like, M1-like, and transforming growth factor–β–positive (TGF-β$^+$) M2-like macrophages, whereas it showed a substantial decrease after Exo-srIκB treatment in M0-like and TGF-β$^+$ M2-like macrophages (Fig. 4G). Compared with those in the saline group, the up-regulated DEGs of the four macrophage subtypes in the LPS group were associated with biological processes such as myeloid leukocyte activation, leukocyte chemotaxis, and cytokine production, suggesting an increase in cellular processes related to classical activation of macrophages. Compared with those in the LPS-stimulated group, the down-regulated DEGs in the Exo-srIκB–treated group were associated with processes such as leukocyte activation, chemotaxis, and response to molecules of bacterial origin, suggesting that Exo-srIκB treatment suppressed many cellular signaling pathways that were activated by LPS (fig. S8, A and B). In addition, we assessed the changes in activation signatures of B, T, and NK cells across the three conditions (fig. S9). Our analysis showed no significant increase in the mean activation scores exceeding the baseline expression levels of control genes (equivalent to a score of 0) in any of these cells following LPS stimulation, consistent with the minimal differential expression observed between saline- and LPS-treated groups in these cells (see Fig. 4A and fig. S5A). The results indicate that, in contrast to innate immune cells, adaptive immune cells did not exhibit significant changes in our LPS-induced chorioamnionitis model.

To verify that the observed differential gene expression of neutrophils and macrophages across the three conditions was driven by NF-κB signaling, we examined the expression levels of representative target genes of canonical NF-κB signaling. As expected, the expression of these genes was increased in neutrophils and macrophages, particularly in Neu1, Neu2, M0-like, and M1-like macrophages, after LPS stimulation compared with that in the saline-injected group. Conversely, Exo-srIκB treatment led to a reduction in the expression of these genes (Fig. 4H). Furthermore, to evaluate the changes in the transcriptional regulatory networks governed by NF-κB across the three treatment groups, we applied the SCENIC (single-cell regulatory network inference and clustering) method (*53*) to decidua immune cells. Among the five NF-κB family TFs (*NFKB1*, *NFKB2*, *REL*, *RELA*, and *RELB*) (*54*), we identified three (*NFKB1*, *NFKB2*, and *REL*) from a total of 473 regulons. Initial evaluation of the regulon activities of these three NF-κB family TFs indicated that the activity of the *NFKB1* regulon was high in neutrophils and macrophages, highlighting a central role of the canonical NF-κB signaling in the activation of innate immune cells in chorioamnionitis (Fig. 4I). A comparison of the activities of NF-κB–related regulons across the three conditions demonstrated that LPS prominently increased their activities in neutrophils and some macrophage subtypes (specifically M0-like and M1-like macrophages). Conversely, Exo-srIκB treatment reduced the activities of regulons, especially those of *NFKB1* and *REL*, which represent the canonical signaling and main targets of the drug, in all neutrophils and macrophage subtypes, with the effect being more prominent in M0-like and TGF-β$^+$ M2-like macrophages (Fig. 4J). Furthermore, we assessed the changes in the mitogen-activated protein kinase (MAPK) and Janus kinase (JAK)/signal transducers and activators of transcription (STAT) pathways in innate immune cells, which may also be activated by LPS administration (*55*–*57*). Our analysis revealed that the MAPK pathway activity score was significantly elevated in M1-like and IL-10$^+$ M2-like macrophages following LPS stimulation. Conversely, these activations were significantly suppressed by Exo-srIκB administration (fig. S10, A and B). In addition, several regulons regulated by TFs downstream of the MAPK pathway were identified in our data and observed to be activated upon LPS stimulation, particularly in M0-like and M1-like macrophages. The activities of *MAPK1*, *CREB1*, *ATF2*, and *MEF2A* regulons were reduced upon Exo-srIκB administration in M0-like macrophages, while they remained mostly unaffected in other cell types (fig. S10C). The activities of *STAT2*, *STAT3*, and *STAT5B* regulons in the JAK/STAT pathway were increased following LPS stimulation in all innate immune cell types. However, these activities were markedly reduced by the coadministration of Exo-srIκB only in M0-like macrophages, without affecting other cell types (fig. S10D). Exo-srIκB does not predominantly target the MAPK and JAK/STAT pathways, resulting in its limits in fully regulating these pathways. The regulation observed in specific macrophage subtypes may be ascribed to a general down-regulation of the proinflammatory microenvironment via control of NF-κB signaling. These findings

suggest that the treatment of chorioamnionitis should also consider multiple inflammatory pathways induced by LPS. Together, the analysis of differential expression and activity of the components of NF-κB signaling showed that LPS treatment activated neutrophils and macrophages in the decidua, leading to perturbations in the homeostatic macrophage composition, whereas Exo-srIκB partially alleviated this LPS-induced inflammation and enhanced NF-κB signaling activities, particularly exerting an effect on macrophages.

Alterations in cell-cell communication among immune cells in the decidua

To examine the effects of Exo-srIκB treatment on cellular interactions between different immune cells in the decidual microenvironment, we used CellChat (*58*), an R package that quantitatively analyzes and compares cell-cell interactions using scRNA-seq data from various biological conditions. The analysis of information flow—which refers to the collective sum of communication probabilities within a condition for a particular signaling pathway—demonstrated that proinflammatory pathways such as tumor necrosis factor (TNF), IL-1, and C-C motif chemokine ligand (CCL) were more active in the LPS-treated group compared with those in the saline-injected group (Fig. 5A). Conversely, the information flow of these pathways, except that of CCL, was reduced following Exo-srIκB treatment (Fig. 5B). Extensive assessment and comparison of the interactions between the various immune cell types revealed a significant increase in the interactions from macrophages to neutrophils after LPS stimulation compared with those in the saline-treated group. Conversely, following Exo-srIκB treatment, these interactions were diminished (Fig. 5, C and D). Thus, we focused on the changes in the interactions between macrophages and neutrophils. The interactions of multiple ligand-receptor pairs, specifically directed from macrophages to neutrophils, were significantly increased in LPS stimulation, whereas they were subsequently decreased after Exo-srIκB treatment; these ligand-receptor pairs include *TNF-TNFRSF1B*, *IL1B-IL1R2*, *IL1B*–(*IL1R1* + *IL1RAP*), and *CXCL8-CXCR2* (Fig. 5E and fig. S11, A and B). *TNF*, *IL1B*, and *CXCL8* are recognized as potent activators and chemoattractants for neutrophils in the choriodecidua, leading to uterine inflammation (*20*, *59*, *60*). However, changes in the interactions directed from neutrophils to macrophages were not as prominent as those from macrophages to neutrophils, with considerably fewer changes identified in ligand-receptor pairs across different conditions (fig. S12, A and B). These results substantiated our differential analysis results that Exo-srIκB altered the LPS-stimulated decidua immune microenvironment by primarily influencing and modifying the molecular characteristics of macrophages and their cross-talk with neutrophils.

Effects of Exo-srIκB on LPS-induced inflammation on cynomolgus macaque choriodecidua of the EPMs and amniotic fluid

Considering the positive effects of Exo-srIκB in reducing LPS-induced inflammation in the immune microenvironment of decidua, we investigated whether Exo-srIκB treatment could also alleviate inflammation in the choriodecidua of EPM. Hence, we performed bulk RNA-seq of cynomolgus macaque choriodecidua tissues obtained from nine pregnant cynomolgus macaques injected with saline, LPS, or LPS + Exo-srIκB ($n = 3$ each). We found that the quality control metrics of bulk RNA-seq data were acceptable, with the data from biological replicates exhibiting a strong correlation (fig. S13, A and B). Principal components analysis (PCA) showed that the three treatment groups exhibited distinct transcriptomes (Fig. 6A). Using hierarchical clustering of significant DEGs, we identified four distinct patterns (Fig. 6B). Pattern 1 genes refer to those DEGs whose expression was initially elevated in response to LPS stimulation relative to saline and then down-regulated after Exo-srIκB treatment. These genes (pattern 1) were found to be associated with GO biological processes and Kyoto Encyclopedia of Genes and Genomes (KEGG) pathways, including cytokine production, myeloid leukocyte activation, response to molecule of bacterial origin, chemokine signaling, and NF-κB signaling pathway. This finding suggested that LPS stimulation induced choriodecidual inflammation, which was subsequently alleviated by Exo-srIκB treatment (Fig. 6, C and D). In addition, gene set variation analysis (GSVA) revealed that LPS-induced inflammation, along with the associated signaling pathways (Toll-like receptor 2 or 4 signaling pathways) and corresponding myeloid leukocyte responses (myeloid leukocyte activation, migration, and cytokine production), was consistently up-regulated in all LPS-treated samples. However, these responses were down-regulated in two of three samples upon treatment with Exo-srIκB (Fig. 6E). These results indicated that Exo-srIκB treatment effectively reduced LPS-induced choriodecidua inflammation.

Next, we evaluated the inflammatory cytokine levels in the amniotic fluid to assess the effects of LPS stimulation and Exo-srIκB treatment (fig. S14). The levels of all the examined cytokines tended to increase after LPS stimulation compared with those in the saline-injected group, whereas most cytokine levels, except those of IL-6, tended to decrease following Exo-srIκB treatment compared with those in the LPS-injected group. However, these trends were not statistically significant, possibly due to the small sample size ($n = 3$ per group).

Intraamniotic LPS injection did not induce systemic inflammation in maternal cynomolgus macaques

Our data provided compelling evidence that intraamniotic LPS administration caused inflammation in the choriodecidua of the placenta. Nevertheless, we questioned whether the direct delivery of LPS into the amniotic cavity also induced systemic inflammation in maternal cynomolgus macaques. To determine this, we performed scRNA-seq on matched peripheral blood mononuclear cells (PBMCs) obtained from six cynomolgus macaques injected either with saline, LPS, or LPS + Exo-srIκB ($n = 2$ each); their decidua tissues were also subjected to scRNA-seq. We assessed the quality control metrics and filtered out the low-quality cells, leaving a total of 5492 cells for downstream analysis (saline, 2369 cells; LPS, 3669 cells; LPS + Exo-srIκB, 1587 cells; Fig. 7A and fig. S15). We identified 11 cell types based on their expression of established marker genes (Fig. 7B). We found that the monocyte population increased in one of the LPS-treated cynomolgus macaques compared with that in the saline-treated animals; however, this trend was not consistent across individuals. The other cell types displayed negligible alterations (Fig. 7C). Given that monocytes have been identified as the primary cell type responding to LPS treatment in PBMCs (*61*), we proceeded to examine the characteristics of monocytes under the three experimental conditions. Analysis of the classical activation score of monocytes showed that the level of activation for both classical and nonclassical monocytes remained unchanged after LPS stimulation compared with that after saline treatment (Fig. 7D). In addition, differential expression analysis

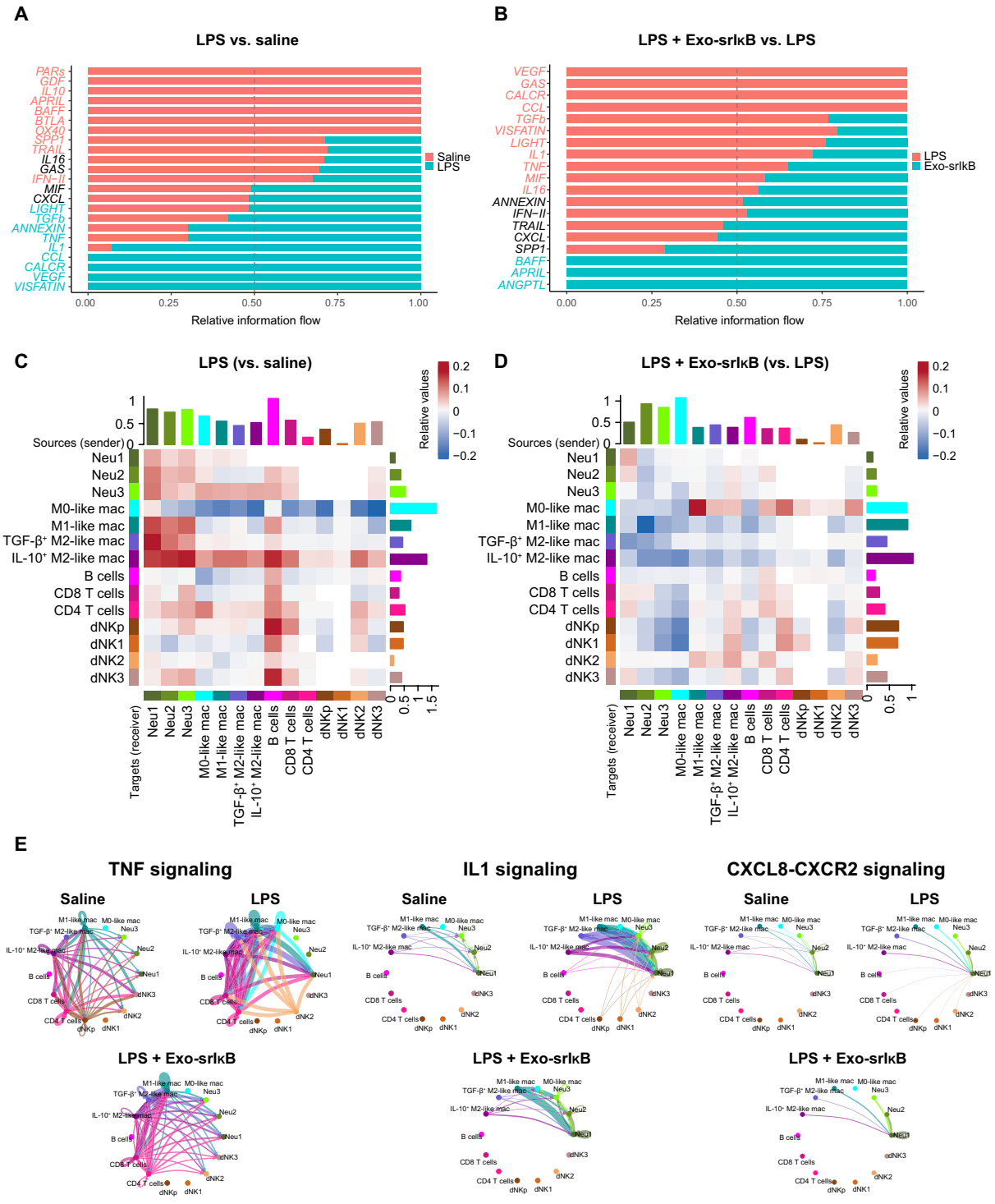

Fig. 5. Cell-cell interactions between immune cells within the three different groups. (**A** and **B**) Signaling pathways exhibiting greater differences in the overall information flow within the inferred networks, among immune cells between LPS- and saline-injected groups (A) and between LPS + Exo-srIκB– and LPS-injected groups (B). Cumulative communication probabilities within a network were summed to determine the overall information flow of a particular signaling pathway. Pathways highlighted in red showed higher level of enrichment in saline-injected (A) or LPS-injected (B) groups; pathways highlighted in green exhibited higher level of enrichment in LPS-injected (A) or LPS + Exo-srIκB–injected (B) groups. (**C** and **D**) Heatmap displaying differences in interaction strength among different types of immune cells between the LPS- and saline-injected groups (C) and between the LPS + Exo-srIκB– and LPS-injected groups (D). Red indicates higher interaction strengths, whereas blue indicates reduced interaction strengths between particular cell types in LPS-injected (C) or LPS + Exo-srIκB–injected (D) groups. Bar plots (top) represent the sum of column values, indicating incoming signaling; bar plots (right) represent the sum of row values, indicating outgoing signaling. (**E**) Circle plots showing cell-cell interactions in specific signaling pathways. Edge colors indicate sources of signaling; edge widths are proportional to the interaction strength between two cell types.

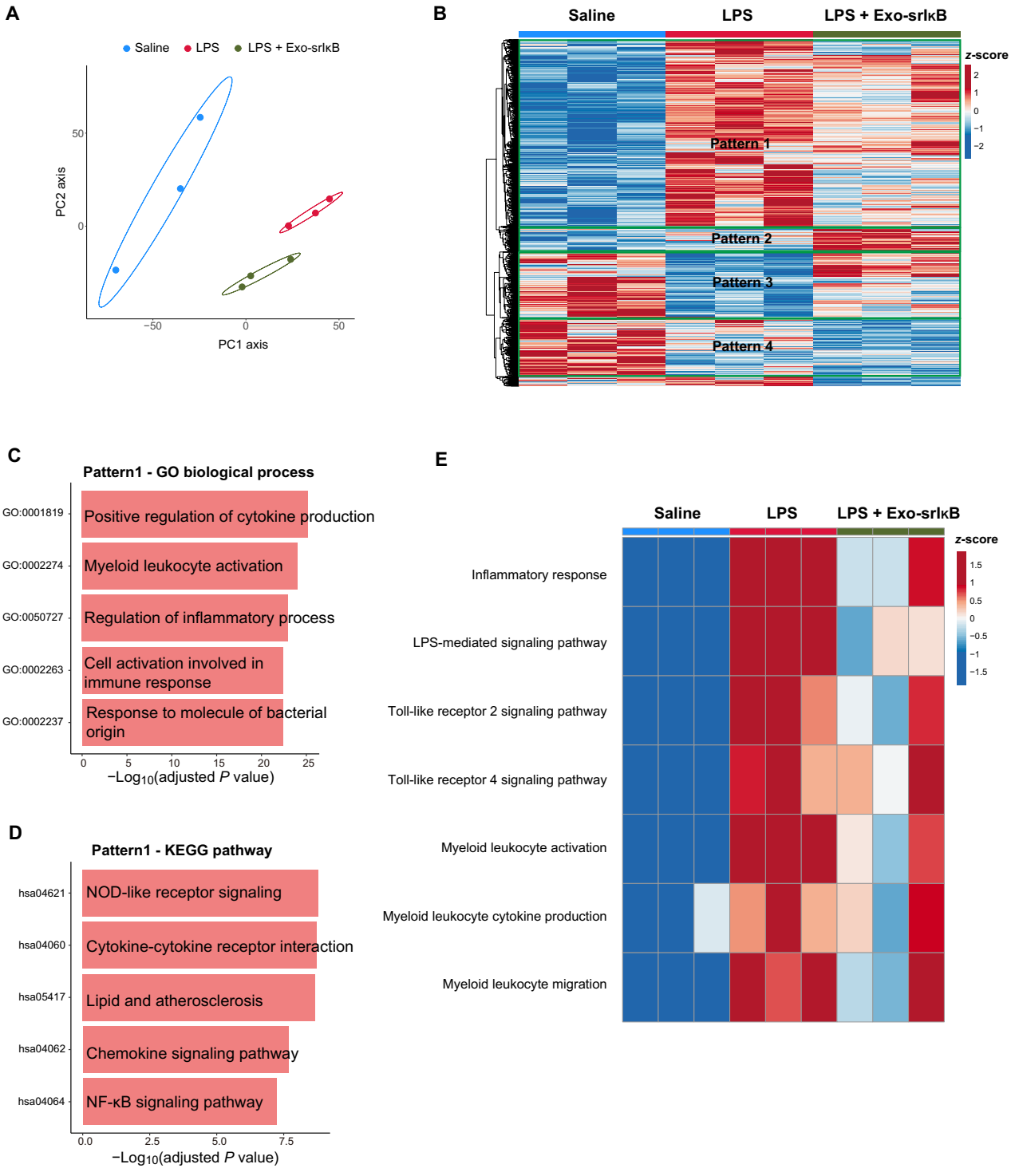

Fig. 6. Bulk RNA-seq of cynomolgus macaques choriodecidua of EPMs. (**A**) PCA plot of bulk RNA-seq data. (**B**) Heatmap depicting the results of hierarchical clustering of significant DEGs among the three treatment groups. Genes with Benjamini-Hochberg–adjusted $P < 0.05$ were defined as significant DEGs. Clustering revealed four distinct expression patterns. Colors in the heatmap represent the *z*-scored, normalized expression values. (**C** and **D**) Top 5 GO biological process (C) and KEGG pathway (D) terms with Benjamini-Hochberg–adjusted $P < 0.05$, ordered by $-\log_{10}$ (adjusted *P* value), enriched in DEGs belonging to pattern 1. NOD, nucleotide-binding oligomerization domain. (**E**) Heatmap representing the results of GSVA. Columns indicate samples; rows indicate each tested gene set. Colors represent the *z*-scored, normalized enrichment scores.

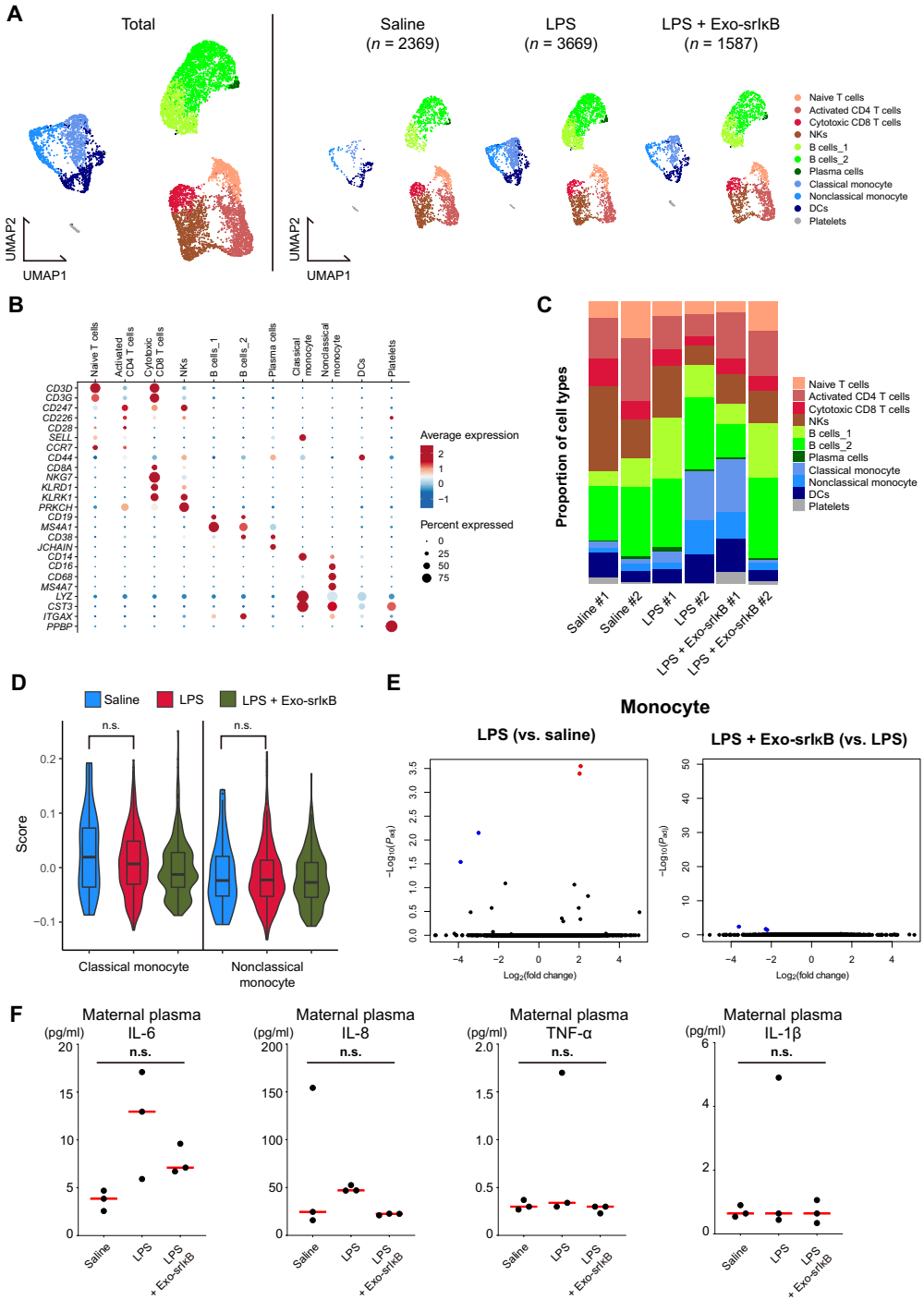

Fig. 7. scRNA-seq of maternal cynomolgus macaque PBMCs. (**A**) UMAP plots of maternal PBMC scRNA-seq data, composed of 7625 cells (saline, 2369 cells; LPS, 3669 cells; LPS + Exo-srIκB, 1587 cells). DCs, dendritic cells. (**B**) Dot plot showing the expression of marker genes used for the identification of each cell type. Dot color and size represent *z*-scored, normalized expression values and percentage of cells expressing a specific gene, respectively. (**C**) Bar plots showing the proportion of cell types in each individual animal. (**D**) Violin plots depicting the monocyte classical activation signature score among the three treatment groups within classical and nonclassical monocytes. *P* values were calculated using one-way ANOVA with Bonferroni correction for multiple comparisons. (**E**) Volcano plots showing the results of differential expression analysis in monocytes between two indicated groups. Genes are plotted using the $\log_2$(fold change) (*x* axis) and $-\log_{10}$[adjusted *P* value (P_{adj})] (*y* axis). Significantly up-regulated genes are colored in red, down-regulated genes are in blue, and insignificant genes are in black. Genes with Benjamini-Hochberg–adjusted $P < 0.05$ were considered significantly differentially expressed. (**F**) Cytokine levels in the maternal plasma across the three treatment groups were assessed using a multiplex ELISA. IL-6 levels were increased in the LPS group compared with those in the saline group; however, the difference was not statistically significant. The levels of other cytokines were similar among the three groups. Data are presented as median with individual values ($n = 3$ biological replicates per group). Kruskal-Wallis test was performed to determine statistical significance.

revealed the presence of very few significant DEGs between the LPS and saline treatments as well as between the LPS + Exo-srIκB and single LPS treatments in monocytes (Fig. 7E). These results indicated that the intraamniotic administration of LPS did not elicit any significant responses in the systemic circulation of mother cynomolgus macaques. We further confirmed these results by examining the inflammatory cytokine levels in the maternal plasma using a multiplex enzyme-linked immunosorbent assay (ELISA). In the maternal plasma, only IL-6 levels showed an increasing trend, without statistical significance, in the LPS-injected group compared with those in the saline group. The levels of all other cytokines remained similar regardless of LPS stimulation (Fig. 7F). Overall, these findings implied that the observed changes in the immune microenvironments of choriodecidua were attributed to the localized activity of LPS and Exo-srIκB.

Blockade of NF-κB signaling by Exo-srIκB alleviated the LPS-induced fetal lung injury

As chorioamnionitis induces a proinflammatory milieu in the amniotic fluid, which directly flows into the fetal lung in utero (*62*), this inflammatory microenvironment triggers massive immune cell infiltration and perturbs the normal developmental process of the fetal lung (*63*). Therefore, as Exo-srIκB efficiently mitigated the LPS-induced chorioamnionitis, we further explored its efficacy against LPS-induced fetal lung injury by evaluating autopsied lungs of neonates immediately after the cesarean section. Compared with that in the saline-injected group, intraamniotic LPS injection induced a marked infiltration of immune cells and the destruction of alveolar space architecture (Fig. 8, A and B). Conversely, when Exo-srIκB was administered following LPS stimulation, the massive infiltration of immune cells and devastation of normal tissue structure were markedly diminished, as evidenced by a significantly reduced neonatal lung injury score compared with that after LPS stimulation (Fig. 8, C and D). Multiplex ELISA of inflammatory cytokines in homogenized frozen fetal lung tissues from the three groups reflected the trends observed in immunohistochemical analyses, although the changes did not reach statistical significance due to the small sample size (Fig. 8E). Furthermore, the expression levels of inflammatory cytokines in fetal cord plasma from available animals (saline, $n = 3$; LPS, $n = 2$; LPS + Exo-srIκB, $n = 2$) (fig. S16) displayed similar trends to those observed in fetal lung tissues.

Gliosis and neuroinflammation were not induced in the white matter and cerebellum of fetuses exposed to intraamniotic LPS

Since near-term fetuses swallow substantial amounts of amniotic fluid, intraamniotic LPS can be absorbed systemically through the gastrointestinal tract, potentially triggering neuroinflammation. To test this, we performed immunohistochemical staining for microglia (IBA-1), astrocyte [glial fibrillary acidic protein (GFAP)], and TNF-α to identify the presence of gliosis and neuroinflammation in fetal brains from the three groups. Through these analyses, we found no notable differences across the three groups in the intensity or pattern of IBA-1, GFAP, and TNF-α expression in the fetal periventricular white matter (PVWM) and cerebellum (fig. S17). This indicates that no prominent neuroinflammation was induced in the fetus by intraamniotic LPS exposure.

DISCUSSION

Exo-srIκB treatment reduced the proinflammatory responses in the macrophages and neutrophils of decidua, resulting in the attenuation of neutrophil recruitment to choriodecidua

Regarding intrauterine infection, which is an important underlying cause of spontaneous PTB, the recruitment and activation of neutrophils to the choriodecidua, which are main components of the pathophysiology of chorioamnionitis, are orchestrated through the function of a cascade of inflammatory cytokines and mediators under the governance of NF-κB signaling (*64*). Elevated levels of cytokines, such as IL-1, IL-6, TNF-α, and prostaglandins, are typically observed in such conditions; notably, IL-1 is a critical mediator in amplifying the inflammatory response and orchestrating the recruitment of neutrophils to the choriodecidua (*20*, *59*). The present study advances the understanding of anti-inflammatory strategies by demonstrating that anti-inflammatory exosomes specifically engineered to carry a super-repressor for NF-κB can effectively attenuate the recruitment of neutrophils in the choriodecidua of pregnant NHPs. In addition, a concomitant reduction was observed in the expression of proinflammatory genes largely governed by NF-κB in macrophages and neutrophils.

Controversy regarding the predominant role of macrophages in LPS-induced chorioamnionitis and the contribution of M2 macrophages to neutrophil activation

The role of macrophages in the activation of neutrophils during chorioamnionitis, particularly in the choriodecidua, has not been fully explored. This gap in knowledge could be attributed to the specialized nature of the choriodecidua as part of the maternal-fetal interface and the complexity of immune interactions during pregnancy-related conditions. Our data indicated that activated macrophages are the primary cells responsible for activating the inflammatory response of neutrophils, underscoring their central role in detecting and responding to chorioamnionitis. This finding contrasts slightly with the conventional view that neutrophils play the dominant role in chorioamnionitis (*65*) and highlights the complexity of immune regulation at the maternal-fetal interface. Decidual M1-like macrophages are known to be associated with spontaneous preterm labor in humans (*66*). We observed that not only the proinflammatory M1 macrophages but also M2 macrophages, which are typically associated with anti-inflammatory responses, contributed to the activation of neutrophils through the TNF and IL-1 signaling pathways. This finding challenges the conventional dichotomy of macrophage polarization and suggests a more nuanced role for M2 macrophages in the pathogenesis of chorioamnionitis. Hofbauer cells, which are specialized placental macrophages, typically exhibit an M2 phenotype and are primarily involved in tissue maintenance and repair (*67*). However, their role in chorioamnionitis remains controversial, possibly unrelated (*68*), hindering (*69*), or contributing to the proinflammatory milieu (*70*, *71*). Notably, all these previous studies (*69*, *71*), except one (*70*), focused on the villi of the placental disc but not on the choriodecidua, which is the most important tissue for studying chorioamnionitis. While our data suggest that macrophages may play a more pronounced role than neutrophils in regulating LPS-induced chorioamnionitis and indicate the potential involvement of Hofbauer cells in neutrophil activation, these connections remain unconfirmed and warrant further detailed investigation in future studies.

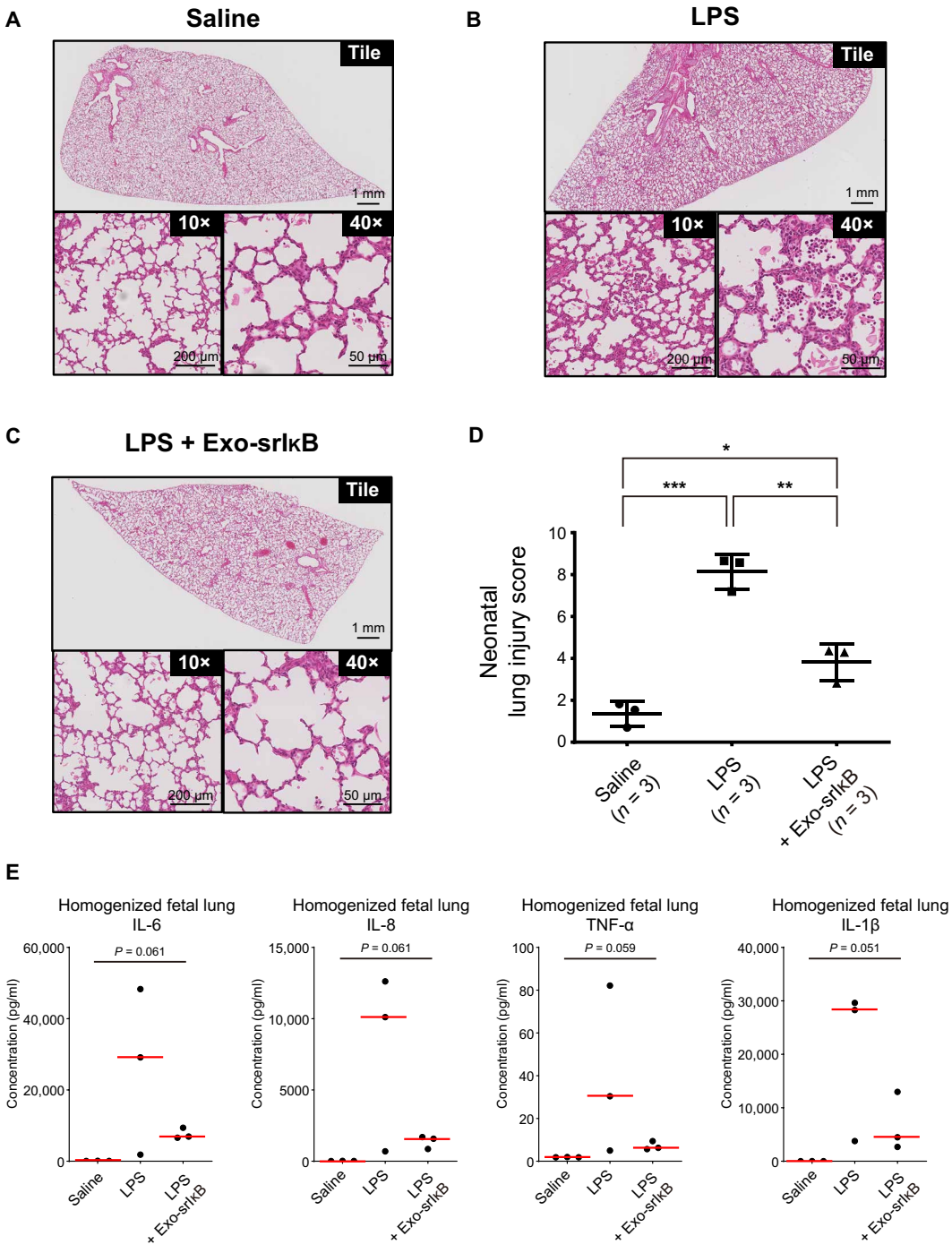

Fig. 8. Mitigation of LPS-induced fetal lung inflammation following Exo-srIκB administration. (**A** to **C**) Histological examination of fetal lung injury across the three treatment groups. [i.e., saline (A), LPS (B), and LPS + Exo-srIκB (C)]. (**D**) Neonatal lung injury score calculated on the basis of ATS criteria (0 to 10 range). Data are presented as means ± SDs ($n = 3$ biological replicates per group). A one-way ANOVA with Tukey's correction for multiple comparisons was performed to determine statistical significance. $^{*}P \leq 0.05$, $^{**}P \leq 0.01$, and $^{***}P \leq 0.001$. (**E**) Cytokine levels in homogenized frozen fetal lung tissues assessed by multiplex ELISA. Data are presented as median with individual values ($n = 3$ biological replicates per group). Kruskal-Wallis test was performed to determine statistical significance among the three groups, with the calculated P value indicated in the plots.

Which route of LPS administration is more appropriate for a chorioamnionitis model?

Ascending intrauterine infection is a major etiology of spontaneous PTB. It is traditionally well known that intrauterine infection, originating from the vaginal and cervical canals, ascends to the choriodecidua and amnion in EPM, ultimately leading to fetal infection (*6*). On the basis of these traditional concepts, it seems appropriate to inject the LPS either into the vagina or the choriodecidual space. However, an important previous study demonstrated that bacteria were more frequently detected in the amniotic fluid than in the chorioamniotic membranes in cases where microbes invade amniotic cavity. In addition, 16*S* ribosomal RNA gene copy numbers were significantly higher in the amnion compared to the chorion across all groups with chorioamnionitis of stages 0 to 3 (*72*). The study proposed a model in which the initial stage of chorioamnionitis involves intraamniotic bacterial invasion through a discrete region of the chorioamniotic membranes, followed by intraamniotic proliferation, with bacterial invasion of chorioamniotic membranes primarily extending from the amniotic fluid. Therefore, we reasoned that the intraamniotic route of LPS injection is more appropriate than the choriodecidual route, which is consistent with multiple previous publications studying chorioamnionitis in NHP (*20*, *41*, *42*).

Exo-srIκB showed potential as a treatment for chorioamnionitis in both mouse and NHP models

Progesterone is solely used to diminish spontaneous PTB in pregnant women at high risk for PTB before the gestational age of 34 weeks (*73*), rather than serving as a definitive treatment to alleviate inflammation within the uterus. Moreover, the specific biological pathways through which progesterone prevents PTB in humans have not yet been thoroughly elucidated, although various potential mechanisms have been suggested (*74*, *75*). Notably, our study highlighted Exo-srIκB as a potential therapeutic agent capable of addressing the foundational inflammatory processes within the uterine environment such as choriodecidua in an NHP preterm chorioamnionitis model. Consistent with these observations, we have previously shown that Exo-srIκB delayed LPS-induced PTB by modulating the choriodecidual inflammatory response and NF-κB activation in a mouse model, which parallels the inflammatory process observed in chorioamnionitis (*35*). However, for pregnancy-related disease models such as chorioamnionitis, NHPs are a more appropriate translational model than rodents. This is because NHPs, particularly cynomolgus macaques, have a singleton pregnancy similar to that in humans, in contrast to rodents that typically have multiple pregnancies. In addition, NHPs have anatomically and histologically comparable uterine structures to those of humans (one fundal cavity with a hemomonochorial histological type) as opposed to rodents (didelphys structure with a hemotrichorial histologic type). Moreover, a recent study found a notable similarity in the transcriptomic profiles of chorioamnionitis between NHPs and humans (*76*), suggesting that the beneficial effects of Exo-srIκB demonstrated in this study may directly apply to humans with the same conditions. These exosomes effectively reduced choriodecidual inflammation in rodents and NHPs, highlighting the therapeutic potential of exosome-based interventions for intrauterine inflammatory conditions in humans.

A direct and local effect of intraamniotic LPS on fetal lungs, rather than a secondary effect of choriodecidual inflammation

A previous sheep PTB model shows that direct exposure of LPS to fetal lungs via the intratracheal route, as well as through the chorioamnion, can induce a fetal inflammatory response (*77*). Moreover, Toth *et al.* (*63*) have demonstrated that intraamniotic anti–IL-1 therapy mitigates LPS-induced fetal lung injury in a rhesus PTB model similar to ours. Therefore, the effects observed in the fetal lungs in our study are likely due to the direct effects of intraamniotic LPS and Exo-srIκB rather than the secondary effects mediated through the regulation of choriodecidual inflammation. Furthermore, this may explain the consistent therapeutic effects of Exo-srIκB observed in all three fetuses from this study. Given that ~170 cm^3 of amniotic fluid reaches the fetal lungs daily in near-term fetuses (*78*), it is expected that LPS or exosomes present in the amniotic fluid exert a direct and localized effect on the fetal lungs. Further studies will be needed to validate these findings.

Limitations and future perspectives

Because of limited animal availability, we were unable to examine the effect of different injection timings (e.g., prophylactic versus postintervention). In our study, Exo-srIκB was administered to the maternal side concurrently with intraamniotic LPS stimulation, at a later time point than in previously reported models, which provided therapeutic agents 3 hours before LPS stimulation (*20*, *63*). Given the extensive vascularization of the decidua and the anticipated accumulation of exosomes in inflamed tissues (*79*–*81*), we hypothesized that Exo-srIκB could mitigate inflammation in the EPM even when administered simultaneously with LPS stimulation. Although we anticipate that a preventive approach will continue to be effective against chorioamnionitis due to the prolonged intracellular presence of srIκB, this hypothesis has not yet been validated. Likewise, whereas our previous study in a preclinical sepsis model indicated that Exo-srIκB administration up to 6 hours post–LPS injection had therapeutic benefits, further studies are necessary to ascertain if such a delayed intervention is similarly effective in chorioamnionitis (*36*). Moreover, comprehensive biodistribution studies in an NHP model are necessary to differentiate the effects of intravenous and intraamniotic injections on therapeutic efficacy. Our previous studies on mice and rats indicated that most intravenously administered exosomes accumulate in the liver (50 to 70%), with further localization in the spleen and lungs (*82*), and showed that exosomes can traverse the placental barrier (*83*). Despite their primary distribution to filtration organs, intraperitoneal injection of Exo-srIκB effectively extended gestation by over 24 hours and mitigated choriodecidual inflammation following LPS stimulation in a murine model (*35*). Nonetheless, these findings may not fully align with the complex physiology of the cynomolgus macaque. This study involved the administration of Exo-srIκB through both intravenous and intraamniotic routes to enhance the therapeutic efficacy from maternal and fetal perspectives in this study; however, further research is required to clarify the relative contributions of these dual therapeutic approaches on inflammation in the choriodecidua. Furthermore, while our therapy targets inflammation, NF-κB also plays a role in fetal development, pregnancy maintenance, and the labor process (*84*, *85*). While our intervention is intended for application during the late stages of fetal development, when crucial organogenesis dependent on NF-κB is mostly complete; nonetheless, repeated administration of Exo-srIκB may lead to

sustained NF-κB inhibition. This prolonged inhibition may influence the final stage of developmental processes, especially in the lungs (*86*, *87*). Given that NF-κB facilitates surfactant synthesis and lung epithelial cell function, extended inhibition may theoretically postpone lung maturation in preterm neonates. While some NF-κB inhibitors, including sulfasalazine—an IκB kinase inhibitor used to treat inflammatory bowel disease and rheumatoid arthritis (*88*)—are considered as relatively safe for use during pregnancy (https://reprotox.org/member/agents/29867), further long-term safety assessments are required to ascertain that the therapeutic benefits of Exo-srIκB do not compromise newborn health. Another weakness of our study is the resource limitations regarding the number of experimental monkeys available for the study. To achieve statistical validity, we decided to include three animals per group (i.e., saline, LPS, and LPS + Exo-srIκB), rather than having one or two animals per group across five conditions (i.e., saline, Exo-srIκB alone, LPS, LPS + Exo-naïve, and LPS + Exo-srIκB). However, it is important to consider that animal models of prenatal inflammation, particularly NHP, often exhibit substantial interindividual variability. Although we assigned a minimum of three animals per group, one animal (Exo-srIκB 3 in table S1) displayed a quite different response in the histopathologic examination of the EPM, amniotic fluid cytokine levels, and choriodecidua bulk RNA-seq GSVA results compared to the rest of the LPS + Exo-srIκB group (Figs. 1D and 6E and fig. S14). Another important consideration is that although the Exo-srIκB might have exerted its anti-inflammatory effects simply by diluting the concentration of LPS in the amniotic fluid, the protective effect of Exo-srIκB in the current study should not be attributed to dilutional effects for the following reasons: (i) We injected the same volume (3 ml) of normal saline intraamniotically in the LPS-alone group as in the LPS + Exo-srIκB group, which received 3 ml of intraamniotic Exo-srIκB administration; and (ii) intraamniotic Exo-srIκB injection was conducted 1 hour after the intraamniotic LPS stimulation. Last, the implementation of our Exo-srIκB treatment in human clinical settings at risk of spontaneous PTB may be constrained by the lack of early noninvasive diagnostic tools for chorioamnionitis, alongside the difficulty in distinguishing *Escherichia coli* from other pathogens, such as group B *Streptococcus* (GBS) infection. Consequently, it is imperative to evaluate our therapeutic approach in other pathogenic situations, such as in GBS-induced chorioamnionitis (*89*), which encompasses mechanisms beyond the Toll-like receptor 4 signaling.

Overall, our findings, alongside evidence from diverse inflammatory response analyses, endorsed the therapeutic potential of exosome-based interventions in modulating immune responses in chorioamnionitis. These strategies could serve as a blueprint for developing innovative treatments for chorioamnionitis by targeting key inflammatory pathways and cellular interactions.

MATERIALS AND METHODS

Experimental design

This study aimed to assess the therapeutic efficacy of Exo-srIκB in treating chorioamnionitis in an NHP model. Animals were not excluded, randomized, or blinded in the experimental assignment process. All experimental procedures used in this study were approved by the Institutional Animal Care and Use Committee of the Korea Research Institute of Bioscience and Biotechnology (permission number KRIBB-AEC-22055). All drug injections and cesarean section procedures for cynomolgus macaque (*Macaca fascicularis*) were performed by a single surgeon (C.-W.P.) following the Standard Operation Procedures of the Primate Resources Center (Korea Research of Institute Bioscience and Biotechnology). Each experiment was carried out using biological replicates, as indicated by "*n*" in the results section.

Animals

Healthy male ($n = 2$) and female ($n = 9$) cynomolgus macaques, aged 6 to 9 years, were obtained from a facility (Primate Resources Center, Korea Research of Institute Bioscience and Biotechnology) dedicated to NHPs and established as experimental animals in accordance with US/EU NHP indoor group housing guidelines. Animals were fed fresh seasonal fruits and commercial monkey feed (Teklad, global 20% protein primate diet). During the study, animals were cared for by professional veterinarians and caretakers. All animals used in this study were naïve monkeys that had never been used in any other drug tests.

Fertile females and males were selected; pregnancy of nine litters was confirmed through ultrasound (high-resolution ultrasonography machine equipped with a 12.0-MHz probe; LOGIQ e, GE Healthcare Technologies Inc., Chicago, IL, USA) examination following natural mating of two male and nine female monkeys. Gestational days were calculated on the basis of ultrasound examinations. We induced a cynomolgus macaque preterm chorioamnionitis model as previously reported for rhesus macaques (*20*, *41*, *42*). Briefly, pregnant cynomolgus macaques at approximately gestational day 130 (~80% of term gestation) were injected with either 3 ml of saline (Dai Han Pharm, Seoul, Republic of Korea) (saline-treated group, $n = 3$) or 1 mg of LPS (from *E. coli* O111:B4, catalog no. L2630-10 mg, Sigma-Aldrich, St. Louis, MO, USA) in 3 ml of saline solution (LPS-treated group, $n = 3$) via ultrasound-guided intraamniotic injection. Similarly, intravenous [a total of 4×10^{11} pn (9.8×10^{10} pn/kg, considering the weight of monkey as 4 kg)] and intraamniotic [a total of 6.9×10^{10} pn (9.8×10^{10} pn/kg, considering the weight of the fetus, amniotic fluid, and placenta as 0.7 kg)] injections of Exo-srIκB were given to the pregnant cynomolgus macaques at the same time and 1 hour after intraamniotic LPS injection, respectively (Exo-srIκB–treated group, $n = 3$). The selected exosome dosage was extrapolated from the human equivalent dose (3.2×10^{10} pn/kg), adjusted for the relative body weight scale to achieve a comparable dose in cynomolgus macaques. When administering the intraamniotic injection of Exo-srIκB in the LPS + Exo-srIκB group, the same volume (3 ml) of saline was also injected in the LPS-alone group to rule out any dilution effects. We delivered the dams through cesarean section at 16 hours after intraamniotic saline or LPS injection. The demographic characteristics of experimental animals are described in table S1. No instances of spontaneous preterm labor, fetal deaths in utero, or fetal adverse effects (except fetal lung inflammation), nor maternal adverse effects (i.e., sepsis), were observed among any of the cynomolgus macaques. An adequate amount of amniotic fluid was obtained from all experimental pregnant cynomolgus macaques via intraoperative amniocentesis. Immediately after cesarean delivery, placenta samples (i.e., EPMs, umbilical cord, placental disc, and decidua) were obtained.

Preparation of Exo-srIκB

Exo-srIκB, engineered exosomes loaded with free form srIκB, was prepared as previously described (*37*, *39*). Briefly, genetically engineered Expi293F cells were cultured in a wave culture system for 4 days and exposed to blue light for payload loading via light-inducible

protein interaction (*32*). The culture medium was centrifuged at 2000*g* for 10 min to remove cells and debris and filtered through a 0.22-μm polyethersulfone filter. The exosomes were subsequently purified through multiple processes, including ultrafiltration, diafiltration, and multimodal resin chromatography. Last, formulation and sterilization filter processes were performed.

Placental preparation

We obtained placental tissues, which included EPMs (i.e., amnion, membranous chorion, and decidua parietalis), umbilical cord, and placental disc including the chorionic plate, for pathologic evaluation and RNA-seq. Notably, we divided the EPM into the amnion and choriodecidua. Subsequently, decidua tissues were scraped from the EPM. These samples were immediately placed into cryotubes, transferred into a liquid nitrogen tank, and then stored in a freezer at −70°C until RNA-seq. Simultaneously, samples were fixed in 10% neutral buffered formalin and embedded in paraffin for hematoxylin and eosin and immunohistochemical staining.

Diagnosis of acute chorioamnionitis in EPMs

Cynomolgus macaque EPM samples were fixed in a 10% formalin solution, dehydrated using an ethanol gradient, cleared with xylene, embedded in paraffin, and cut into 4-μm-thick sections. These sections were then stained with hematoxylin and eosin (Biognost, Zagreb, Croatia) using the Autostainer XL (Leica Biosystems, Wetzlar, Germany). Acute chorioamnionitis was defined as the presence of neutrophil infiltrations in the EPM, following previously published criteria (*90*): (i) grade 1, one focus of at least five polymorphonuclear leukocytes (PMNs; neutrophils); (ii) grade 2, more than one focus of grade 1 inflammation or at least one focus of 5 to 20 PMNs; (iii) grade 3, multiple or confluent foci of grade 2; and (iv) grade 4, diffuse and dense acute inflammation.

Immunohistochemistry of the EPMs

Cynomolgus macaque EPM samples were fixed in a 10% formalin solution, dehydrated using an ethanol gradient, cleared with xylene, embedded in paraffin, and sectioned into 4-μm-thick sections. These sections were then stained with hematoxylin and eosin (Biognost, Zagreb, Croatia) using the Autostainer XL (Leica Biosystems, Wetzlar, Germany). After staining, the sections were scanned using a SCN400F slide scanner (Leica Microsystems, Wetzlar, Germany). Immunohistochemistry for BCL2A1 and NF-κB–p65 was performed as previously described (*20*). Briefly, paraffin-embedded cynomolgus macaque EPM blocks were sectioned and subjected to antigen retrieval through microwave boiling in a citrate buffer, followed by incubation with anti-human BCL2A1 (catalog no. LS-b450, LSBio, Seattle, USA; 1:200 dilution) or anti–NF-κB–p65 (clone: D14E12, Cell Signaling Technologies, MA, USA; 1:400 dilution), dissolved in 10% normal horse serum/0.2% Tween 20 at 4°C overnight. For indirect detection, sections were incubated with a peroxidase-conjugated goat anti-rabbit immunoglobulin G (IgG) antibody (PI-1000-1, Vector Laboratories, Newark, CA, USA; 1:200 dilution) for 30 min at 25°C (room temperature). Staining was visualized using the 3,3′-diaminobenzidine tetrahydrochloride (DAB) substrate. The BCL2A1- or NF-κB–p65–stained slides were scanned using the SCN400F slide scanner (Leica Microsystems).

Digital image analysis

Anti-BCL2A1 and anti–NF-κB–p65 staining patterns in cynomolgus macaque EPM samples were assessed using the open-source quantitative pathology analysis program QuPath (ver. 0.4.4) (*91*). The anti-BCL2A1– and anti–NF-κB–p65–stained EPM slides were uploaded into the QuPath software as a bright-field (H-DAB) image. Initially, a new EPM image was created manually by randomly selecting three regions with a similar area at the inflammatory site—R1 (placental margin edge), R2 (middle portion), and R3 (ruptured margin edge)—with a measured size of ≈40,000 μm^2 in one section, and the number of anti-BCL2A1– or anti–NF-κB–p65–positive cells in the three regions within this section was determined. For detecting anti-BCL2A1– and anti–NF-κB–p65–stained positive cells, positive cell detection was performed using a single-intensity threshold parameter of 0.2 based on previously reported criteria (*92*). We conducted the verification on two to three available anti-BCL2A1–stained blocks (saline group, total 21 regions; LPS group, total 27 regions; LPS + Exo-srIκB group, total 27 regions from $n = 3$ biological replicates per group) and one to seven available anti–NF-κB–p65–stained blocks (saline group, total 21 regions; LPS group, total 27 regions; LPS + Exo-srIκB group, total 27 regions from $n = 3$ biological replicates per group) per individual case using the QuPath digital image analysis. The average value from the total regions across the available blocks was used as the representative value for each biological replicate, and the final group size was set to $n = 3$ per group.

Immunofluorescent staining in the EPMs

Immunofluorescence assay was performed as previously described (*20*). Briefly, paraffin-embedded EPMs were sectioned and subjected to antigen retrieval by microwave boiling in citrate buffer, followed by incubation with anti-CD68 (clone: KP1, catalog no. MA5-13324, Invitrogen), BCL2A1 (clone: b450, catalog no. LS-b450, LSBio), or neutrophil elastase (clone: 6B6B10, catalog no. NBP2-61658, Novusbio) in 10% normal horse serum/0.2% Tween 20 at 4°C overnight. Staining was visualized using fluorescently labeled secondary antibodies (Alexa Fluor 488 and Alexa Fluor 594, Invitrogen; 1:200 dilution) for 1 hour at room temperature in the dark. Nuclear counterstaining was achieved using VECTORSHIELD HardSet mounting medium with 4′,6-diamidino-2-phenylindole (DAPI; Vector Laboratories). Stained slides were imaged on confocal microscopy for colocalization at ×20 and ×40 magnification with 1024 pixel–by–1024 pixel resolution on a Leica STELLARIS 8 upright microscope (Leica Microsystems). Images were collected using a LAS X (Leica Microsystems).

Preparation of decidua cells and surface staining for flow cytometry

Decidua tissue was washed and digested with Dispase II (Invitrogen, Waltham, MA, USA) plus collagenase A (Roche Diagnostics, Basel, Switzerland) for 30 min, followed by deoxyribonuclease I (DNase I; Roche Diagnostics) treatment for another 30 min. Cell suspensions were filtered, and the obtained red blood cells (RBCs) were lysed (*20*, *50*). Decidua cells were suspended in 1 ml of CELLBANKER 2 (catalog no. 11914, Amsbio, Oxfordshire, UK) and stored at −80°C. The frozen decidua cells were thawed by gently swirling the vial in a 37°C water bath. Then, each 1 ml of cells was immediately mixed with 4 ml of prewarmed Dulbecco's modified Eagle's medium–F12 medium (catalog no. 11320033, Invitrogen). The cell suspension was centrifuged at 1300 rpm and 25°C for 5 min. The supernatant was discarded, and the cell pellets were washed twice with 1 ml of cold 1× phosphate-buffered saline (PBS) via centrifugation at 1300 rpm and 4°C for 5 min. A single-cell suspension in cold fluorescence-activated cell sorting (FACS) buffer (catalog no. 420201, BioLegend, San Diego, CA, USA)

was distributed from 100 μl per tube of cell suspension (2×10^5 to ~5×10^5 cells per tube) into 12 mm–by–75 mm plastic tubes. Then, monoclonal antibodies [anti–CD14–fluorescein isothiocyanate (clone: M5E2, catalog no. 301804, BioLegend), anti–CD16-phycoerythrin (clone: 3G8, catalog no. 302008, BioLegend), and anti–CD11b–antigen-presenting cell (clone: M1/70, catalog no. 101212, BioLegend)] were added, and the mixtures were incubated on ice for 20 min in the dark (*93*, *94*). After that, the cells were washed twice with 1 ml of cold FACS buffer via centrifugation at 1300 rpm for 5 min. Then, the cell pellets were resuspended in 0.5 ml of cold FACS buffer, and 5 μl (0.25 μg) per million cells of 7-amino-actinomycin D (7-AAD) viability staining solution (catalog no. 420403, BioLegend) was added to exclude dead cells. The 7-AAD–negative population was used to determine positive staining for each marker. Data were analyzed using the BD FACSDiva 9.6 software (BD Biosciences, Franklin Lakes, NJ, USA).

Cytokine and chemokine multiplex immunoassay in the amniotic fluid and maternal plasma

Cytokine and chemokine levels in the amniotic fluid and plasma were analyzed using commercially available NHP ProcartaPlex Simplex kits for IL-6, TNF-α, IL-8, and IL-1β according to the manufacturer's instructions (Thermo Fisher Scientific, Invitrogen, Waltham, MA, USA). The levels of these cytokines and chemokines were determined using the Bio-Rad Bio-Plex Luminex 200 multiplex assay system (Bio-Rad, Hercules, CA, USA).

Histological analysis of fetal lung tissue and calculation of the neonatal lung injury score

Representative hematoxylin and eosin–stained fetal lung images (40×) from three animals in each experimental group [i.e., saline (60 fields), LPS (60 fields), and LPS + Exo-srIκB (60 fields) groups] were randomly selected for analyzing the neonatal lung injury score. Images were deidentified and scored independently, using parameters [American Thoracic Society (ATS) criteria] established by Matute-Bello *et al.* (*95*), by three independent researchers blinded to the treatment condition of the samples.

Immunohistochemistry of fetal brains

Immunohistochemistry was performed in the fetal brain sections (*96*). Briefly, paraffin-embedded cynomolgus macaque brain tissues were sectioned and subjected to antigen retrieval by microwave boiling in citrate buffer, followed by incubation with anti-GFAP (catalog no. ab4674, Abcam; 1:500 dilution), IBA-1 (catalog no. 17198, Cell Signaling Technology; 1:200 dilution), or anti-TNF-α (catalog no. ab6671, Abcam; 1:200 dilution) in 5% normal horse serum/0.2% Tween 20 at 4°C overnight. For indirect detection, the slides were incubated with a peroxidase-conjugated goat anti-rabbit IgG antibody (catalog no. PI-1000-1, Vector Laboratories; 1:200 dilution) or goat anti-chicken IgY H&L (catalog no. ab6877, Abcam; 1:200 dilution) for 30 min at room temperature. Staining is visualized using a DAB substrate. The stained slide was scanned using the SCN400F slide scanner (Leica Microsystems).

Multiplex cytokine analysis of homogenized frozen fetal lung tissues and fetal cord plasma

For the multiplex cytokines analysis, frozen fetal lung tissues were first homogenized in tissue lysis buffer (Bio-Plex Cell Lysis Kit, catalog no. 171304011, Bio-Rad) containing a protease inhibitor cocktail (Halt Protease Inhibitor Single-Use Cocktail, catalog nos. 78425 and 78430, Thermo Fisher Scientific, Invitrogen). Then, the supernatants were then collected by centrifugation at 4500*g* for 10 min at 4°C. Protein concentrations were determined using the bicinchoninic acid method (BCA Protein Assay Kit II, catalog no. ab287853, Abcam). After the protein assay, we performed multiplex cytokines analysis of the fetal lung lysate and umbilical cord plasma using commercially available NHP ProcartaPlex Simplex kits for IL-6, TNF-α, IL-8, and IL-1β according to the manufacturer's instructions (Thermo Fisher Scientific, Invitrogen). The levels of these cytokines were determined using the Bio-Rad Bio-Plex Luminex 200 multiplex assay system. During the cesarean section, umbilical cord blood could not be collected from one subject in the LPS group, and in one subject in the LPS + Exo-srIκB group, although collected, the volume was insufficient for multiplex cytokine analysis.

Decidual tissue dissociation from EPM and single-cell preparation

Purified decidua cell suspensions from cynomolgus macaque EPM were prepared as previously described (*20*). Briefly, EPM samples were dissected from the placenta and decidua cells were scraped from the EPM. Decidua tissues were washed and digested with Dispase II (Invitrogen) plus collagenase A (Roche Diagnostics) for 30 min, followed by DNase I (Roche Diagnostics) treatment for another 30 min. Cell suspensions were filtered, and RBCs were lysed and prepared for RNA studies. Decidua tissues and matched PBMCs were subjected to scRNA-seq. scRNA-seq was conducted at ROKIT Genomics (Seoul, Korea). Before dissociation, tissues were washed with PBS and minced into 1- to 2-mm pieces. The tissue pieces were then dissociated using the Neural Tissue Dissociation Kit (P) (130-092-628, Miltenyi Biotech, Bergisch Gladbach, Germany) and gentle MACS dissociator (Miltenyi Biotech), following the manufacturer's instructions. Following dissociation, the cell suspension was sequentially passed through 70- and 30-μm strainers to separate cells from cell debris and undigested tissue chunks. Separated cells were washed twice with cold Ca^{2+}- and Mg^{2+}-free 0.04% bovine serum albumin (BSA)/PBS at 300*g* and 4°C for 5 min. Samples were then gently resuspended in cold Ca^{2+}- and Mg^{2+}-free 0.04% BSA/PBS and then counted using a LUNA-FX7 Automated Fluorescence Cell Counter (Logos Biosystems, Gyeonggi-do, South Korea) with an acridine orange/propidium iodide staining mode. Cell viability was further assessed using the dead cells removal kit (130-090-101, Miltenyi Biotech) and MS columns (130-042-201, Miltenyi Biotech) according to the manufacturer's instructions.

Cell multiplexing, library construction, and scRNA-seq

Cell Multiplexing Oligos (CMOs) were used for cell multiplexing based on 10x cell labeling using the CMO protocol (CG000391, 10x Genomics, Pleasanton, CA, USA). Briefly, for each sample, 1×10^6 cells were resuspended in 100 μl of CMOs (PN1000261, 10x Genomics) and incubated for 5 min at 25°C. After incubation, cells were washed twice in chilled wash and resuspension buffer (1% BSA in Ca^{2+}- and Mg^{2+}-free PBS). All samples were resuspended in cold wash and resuspension buffer to a final concentration of 1300 to 1600 cells/μl and then pooled.

scRNA-seq and cell multiplexing libraries were prepared using the 10x chromium controller, Next Gem single-cell 3′ reagent v3.1 kits (PN-1000123, 10x Genomics) and 3′ feature barcode kit (PN-1000262, 10x Genomics) according to the protocol of the 10x Chromium Single Cell′ v3.1 with feature barcode technology for cell multiplexing

(CG000388; 10x Genomics). Briefly, CMO-labeled cells (target recovery 10,000 cells per sample) were mixed with master mix and loaded with single-cell 3′ gel beads and partitioning oil into a single-cell G chip (PN-1000120, 10x Genomics) to generate single-cell gel bead-in-emulsion (GEM). After GEM incubation in a thermal cycler, barcoded full-length cDNA from mRNA and barcoded DNA from the CMO feature barcode were generated. For 3′ gene expression library preparation, polymerase chain reaction (PCR)–amplified full-length cDNA was sequentially subjected to enzymatic fragmentation, end-repair, A-tailing, adaptor ligation, and index PCR. For cell multiplexing library construction, PCR-amplified DNA from CMO feature barcodes was sequentially subjected to index PCR and size selection.

The purified libraries were quantified by quantitative PCR (qPCR) according to the qPCR quantification protocol guide (#KK4854, KAPA Biosystems, Wilmington, MA, USA) and qualified using the Agilent Technologies 4200 TapeStation (Agilent Technologies, Santa Clara, CA, USA). Libraries were sequenced using the HiSeq 4000 platform (Illumina Inc., San Diego, CA, USA), and 150–base pair (bp) paired-end reads were generated. The sequencing depth was ~20,000 read pairs per cell for the 10x gene expression library and 5000 read pairs per cell for the 10x cell multiplexing library.

scRNA-seq data processing

A custom reference file for *M. fascicularis* was created from a reference genome in the FASTA format (v6.0) and a gene annotation file in GTF format (v6.0), both of which were downloaded from the ENSEMBL database, using the CellRanger (v7.1.0) "mkref" command with default settings. Subsequently, the fastq files from scRNA-seq were aligned to the *M. fascicularis* custom reference genome. The generation of a cell barcode—unique molecular identifier (UMI) count matrix—along with the demultiplexing of PBMC samples, was performed using the CellRanger "count" command and CellRanger "multi" command for the decidua and PBMC data, respectively. All downstream analyses were conducted using R (v4.2.1) with the Seurat package (v4.3) (*97*). Low-quality cells were filtered on the basis of the following criteria: number of detected genes > 250, number of UMI counts between 500 and 100,000, percentage of mitochondrial UMI < 20%, and novelty score (defined as the $\log_{10}$ of the number of detected genes divided by the $\log_{10}$ of the number of UMI counts) > 0.8 (*98*). Subsequently, data from different samples were independently normalized using SCTransform (*99*). For PBMC data, during normalization with SCTransform, the "mitochondrial percentage" was also regressed out. The normalized data from different samples were then integrated using canonical correlation analysis, following the steps tailored for SCTrasnform-normalized data provided in Seurat. PCA was conducted using the RunPCA function with the default variable 3000 genes identified via SCTransform. Next, dimensionality reduction was performed with the top 1 to 15 (for decidua) or 1 to 10 (for PBMCs) principal components using the RunUMAP function. Data clustering was conducted using the FindClusters function (resolution of 0.4 for both decidua and PBMC data) using the Louvain algorithm with the same principal components as for the RunUMAP function. Annotation was carried out on the basis of the expression of known marker genes for each cell type. For decidua samples, the following genes were used for annotation: *KRT8* (ENSMFAG00000040972), *WFDC2*, and *SERPINE2* for epithelial cells; *COL1A1*, *COL1A2*, and *COL3A1* for fibroblasts; *CDH5* and *PECAM1* for vascular endothelial cells; *LYVE1* for lymphatic endothelial cells; *CAMP*, *ORM1*, *CXCL8*, and *LYN* for neutrophils; *C1QA*, *C1QC*, *MERTK*, *CD68*, and *CD14* for macrophages; *CD19* and *MS4A1* for B cells; *CD3D*, *CD3E*, and *CD3G* for T cells; and *NKG7*, *NCAM1*, *GZMA*, *GZMB*, and *PRF1* for NK cells. For PBMC samples, the following genes were used for annotation: *CD3D* and *CD3G* for naïve T cells; *CD4*, *CD247*, *CD226*, and *CD28* for activated $CD4^+$ T cells; *CD3D*, *CD3G*, and *CD8A* for cytotoxic $CD8^+$ T cells; $CD3D^{low}$, $CD3G^{low}$, *PRKCH*, and *KLRK1* for NK cells; *CD19* and *MS4A1* for B cells; *JCHAIN* and *CD38* for plasma cells; $CD14^{high}$ and *CD16* $(ENSMFAG00000053018)^{low}$ for classical monocytes; $CD14^{low}$, $CD16^{high}$, *CD68*, and *MS4A7* for nonclassical monocytes; $CD14^{low}$, $CD16^{low}$, *LYZ*, and *CST3* for dendritic cells; and *PPBP* for platelets.

Calculation of the signature score

We used the AddModuleScore function of the Seurat package (v4.3) to calculate scores for specific signatures. This function computes the average normalized expression levels of individual signature gene sets at the single-cell level, after subtracting the aggregated expression of control feature sets. Genes within signature gene sets are grouped on the basis of their average expression, and control features are randomly selected from each group. The lists of input genes for the calculation of neutrophil activation (*100*–*104*), maturation (*103*), and MAPK pathway activity scores (*105*, *106*) are provided in table S2. The genes used for calculating M1 and M2 signatures (*52*) and macrophage/monocyte classical activation scores (*107*, *108*) are listed in data file S1. For comparing inflammatory response, myeloid leukocyte activation, tissue regeneration, B cell activation, T cell activation, and NK cell cytotoxicity scores, we used the following human gene sets from the MSigDB database (www.gsea-msigdb.org/gsea/msigdb/): INFLAMMATORY_RESPONSE (HALLMARK: M5932), MYELOID_LEUKOCYTE_ACTIVATION (GO:0002274), TISSUE_REGENERATION (GO:0042246), B_CELL_ACTIVATION_INVOLVED_IN_IMMUNE_RESPONSE (GO:0002312), T_CELL_ACTIVATION_INVOLVED_IN_IMMUNE_RESPONSE (GO:0002286), and POSITIVE_REGULATION_OF_NATURAL_KILLER_CELL_MEDIATED_CYTOTOXICITY (GO:0045954). Human gene symbols from these gene sets were converted into cynomolgus macaque gene symbols using the getLDS function in the R package biomaRt (v2.54.1) (*109*). Subsequently, the converted orthologous cynomolgus macaque gene symbols were used for computing the scores (data file S1).

Differential expression and GO enrichment analysis

We performed differential expression analysis after pseudobulking to minimize false positives and *P* value inflation (*110*–*112*). Initially, we used the AggregateExpression function from the Seurat package to perform pseudobulking based on samples. Subsequently, we used DESeq2 (v1.38.3) (*113*) to identify DEGs. DEGs with Benjamini-Hochberg–adjusted $P < 0.05$ were considered significant. Q-Q plots were created to identify cell types with a stronger enrichment for DEGs, as inferred from observed *P* values lower than the expected *P* values.

For GO biological process enrichment analysis, the DEGs of cynomolgus macaques (*M. fascicularis*) genes were converted into human genes using the getLDS function in the R package biomaRt (v2.54.1) (*109*). Subsequently, enrichment analysis was conducted with human ontology gene sets using the R package clusterProfiler (v4.6.2) (*114*). GO terms with Benjamini-Hochberg–adjusted $P < 0.05$ were considered significant.

SCENIC analysis

To create a cisTarget database for *M. fascicularis*, we followed the instructions provided by SCENIC (https://github.com/aertslab/create_cisTarget_databases) and the analysis pipeline as described previously (*115*). First, genomic regions of 5 kb upstream from the transcription start sites of all protein-coding genes of *M. fascicularis* were obtained from the ENSEMBL Biomart (www.ensembl.org). Second, as no annotated TF motifs exist for *M. fascicularis*, we used vertebrate motif annotations obtained from JASPAR2024 (https://jaspar.elixir.no). Last, the cisTarget database for *M. fascicularis* was constructed using the create_cistarget_motif_databases.py script from SCENIC with the genomic regions to score and motif annotations.

Next, we proceeded with SCENIC (v0.12.1, a Python implementation of the SCENIC pipeline) (*53*) analysis of decidua immune cells. First, to reduce computation time, the normalized count matrix was filtered to retain genes expressed in at least 1% of cells. Then, the TF-target gene coexpression modules were calculated using the GRNboost2 algorithm. After identifying the coexpression modules, regulons were determined using the above-created cisTarget database for *M. fascicularis* with default parameters. Last, regulon activities were quantified across single cells using AUCell. The generated AUCell value matrix was integrated into the Seurat object of decidua scRNA-seq data, and regulon activities of interest were visualized using FeaturePlot from Seurat (v4.3) and pheatmap (v1.0.12) in R.

Cell-cell communication analysis

Dynamic changes in cell-cell interactions among various cell types in the decidua were assessed using the R package CellChat (v1.6.1) (*58*). To perform interaction analysis in cynomolgus macaques, *M. fascicularis* genes from the decidua single-cell RNA-seq data were converted into orthologous human genes using biomaRt (v2.54.1), as described above. Normalized count data from each treatment group were used to create CellChat objects, and the analysis was conducted following the proposed pipeline for the comparative analysis of multiple datasets using CellChat. CellChatDB.human served as the ligand-receptor interaction database, and only interactions classified as "secretory signaling" in the database were included in the analysis. Interactions involving fewer than 10 cells were excluded.

Bulk RNA-seq and data analysis

In the choriodecidua of EPM, total RNA extraction was performed using the QIAzol lysis reagent (79306, QIAGEN, Hilden, Germany), while clean-up was conducted using an RNeasy mini kit (74106, QIAGEN) following the manufacturer's instructions. Total RNA concentration was calculated using Quant-IT RiboGreen (R11490, Invitrogen). To assess the integrity of the total RNA (RNA integrity number, RIN), samples were run on the TapeStation RNA screentape (5067-5576, Agilent Technologies). Only high-quality RNA preparations, with RIN values greater than 7.0, were used for RNA library construction. RNA-seq was performed at Macrogen (Seoul, Korea). A library was independently prepared with 1 μg of total RNA for each sample using the Illumina TruSeq stranded mRNA sample prep kit (RS-122-2101, Illumina Inc.). The first step in the workflow involved removing the globin mRNA in the total RNA using the GLOBINclear-Human kit. Following this step, the polyadenylate containing mRNA molecules were purified using poly-T–attached magnetic beads. Following purification, the mRNA was fragmented into small pieces using divalent cations under elevated temperature. The cleaved RNA fragments were copied into first strand cDNA using SuperScript II reverse transcriptase (18064014, Invitrogen) and random primers. This was followed by second strand cDNA synthesis using DNA polymerase I, RNase H, and deoxynucleotide triphosphate. These cDNA fragments underwent an end-repair process, addition of a single "A" base, and ligation of adapters. The products were then purified and PCR-enriched to create the final cDNA library. The libraries were quantified using KAPA library quantification kits for Illumina sequencing platforms according to the qPCR quantification protocol and qualified using the TapeStation D1000 ScreenTape (5067-5582, Agilent Technologies). Indexed libraries were then submitted to an Illumina NovaSeq 6000 (Illumina Inc.) platform, and 2× 100-bp paired-end sequencing was performed. The CLC Genomics Workbench 9.5.3 software (QIAGEN) was used to map the fastq reads to the *M. fascicularis* genome in FASTA format (v6, obtained from the ENSEMBL database) and annotated using the *M. fascicularis* gene annotation file in GTF file format (v6, downloaded from the ENSEMBL database).

Bioinformatic analysis of bulk RNA-seq data was conducted using R (v4.2.1). DEGs were identified using the R package DESeq2 (v1.38.3) (*113*). Genes with a Benjamini-Hochberg–adjusted $P < 0.05$ were defined as significant DEGs. Hierarchical clustering of DEGs was performed after normalizing raw counts using the variance stabilizing transformation (VST) method provided by DESeq2 and averaging the Euclidean distance of genes from each other using the R package pheatmap (v1.0.12). GO biological process and KEGG pathway enrichment analyses were performed using the R package clusterProfiler (v4.6.2) (*114*). For both GO and KEGG pathway enrichment analyses, similar to the approach used in the analysis of scRNA-seq data, DEGs of cynomolgus macaque genes were converted into human genes, and the enrichment analysis was carried out using human ontology gene sets and KEGG pathways. GO and KEGG terms with a Benjamini-Hochberg–adjusted $P < 0.05$ were considered significant. GSVA calculates separate enrichment scores for each pairing of a sample and gene set, determining the degree to which the genes in a specific gene set are coordinately up- or down-regulated within a sample. For the gene sets used in GSVA, lists of genes belonging to the following human gene sets were obtained from the MSigDB database: GOBP_INFLAMMATORY_RESPONSE (GO:0006954), GOBP_LIPOPOLYSACCHARIDE_MEDIATED_SIGNALING_PATHWAY (GO:0031663), GOBP_TOLL_LIKE_RECEPTOR_2_SIGNALING_PATHWAY (GO:0034134), GOBP_TOLL_LIKE_RECEPTOR_4_SIGNALING_PATHWAY (GO:0034142), GOBP_MYELOID_LEUKOCYTE_ACTIVATION (GO:0002274), GOBP_MYELOID_LEUKOCYTE_CYTOKINE_PRODUCTION (GO:0061082), and GOBP_MYELOID_LEUKOCYTE_MIGRATION (GO:0097529). Human genes from these gene sets were then converted into cynomolgus macaque genes using the orthologous gene mapping described earlier. GSVA was performed using the R package GSVA (v1.46.0) (*116*). We ran the gsva function with the "method" argument set to "gsva," "kcdf" argument set to "Gaussian," and "mx.diff" set to TRUE to optimize the analysis for the data matrix normalized using the VST method.

Statistical analysis

Statistical analyses were performed using the GraphPad Prism (v6) or R software (v4.2.1). Independent *t* tests or paired *t* tests were conducted for comparisons between two groups, whereas a one-way analysis of variance (ANOVA) or Kruskal-Wallis tests (for data not assuming normal distribution) were used for comparisons involving

three or more groups, with appropriate post hoc multiple comparison corrections (specified in the figure legends).

Supplementary Materials

The PDF file includes:
Figs. S1 to S17
Tables S1 and S2
Legend for data S1

Other Supplementary Material for this manuscript includes the following:
Data S1

REFERENCES AND NOTES

1. J. R. Fowler, L. V. Simon, "Chorioamnionitis," in *StatPearls*, NBK532251 (Treasure Island, 2023).
2. M. Cappelletti, P. Presicce, S. G. Kallapur, Immunobiology of acute chorioamnionitis. *Front. Immunol.* **11**, 649 (2020).
3. R. P. Perkins, S. M. Zhou, C. Butler, B. J. Skipper, Histologic chorioamnionitis in pregnancies of various gestational ages: Implications in preterm rupture of membranes. *Obstet. Gynecol.* **70**, 856–860 (1987).
4. C. W. Park, K. C. Moon, J. S. Park, J. K. Jun, R. Romero, B. H. Yoon, The involvement of human amnion in histologic chorioamnionitis is an indicator that a fetal and an intra-amniotic inflammatory response is more likely and severe: Clinical implications. *Placenta* **30**, 56–61 (2009).
5. R. Romero, M. Mazor, Infection and preterm labor. *Clin. Obstet. Gynecol.* **31**, 553–584 (1988).
6. R. L. Goldenberg, J. C. Hauth, W. W. Andrews, Intrauterine infection and preterm delivery. *N. Engl. J. Med.* **342**, 1500–1507 (2000).
7. C. J. Kim, R. Romero, P. Chaemsaithong, N. Chaiyasit, B. H. Yoon, Y. M. Kim, Acute chorioamnionitis and funisitis: Definition, pathologic features, and clinical significance. *Am. J. Obstet. Gynecol.* **213**, S29–S52 (2015).
8. J. W. Oh, K. C. Moon, C. W. Park, J. S. Park, J. K. Jun, Acute chorioamnionitis and intra-amniotic inflammation are more severe according to outside-in neutrophil migration within the same chorio-decidua. *Taiwan. J. Obstet. Gynecol.* **60**, 639–652 (2021).
9. J. W. Oh, C. W. Park, K. C. Moon, J. S. Park, J. K. Jun, The relationship among the progression of inflammation in umbilical cord, fetal inflammatory response, early-onset neonatal sepsis, and chorioamnionitis. *PLOS ONE* **14**, e0225328 (2019).
10. J. S. Seong, C. W. Park, K. C. Moon, J. S. Park, J. K. Jun, Necrotizing funisitis is an indicator that intra-amniotic inflammatory response is more severe and amnionitis is more frequent in the context of the extension of inflammation into Wharton's jelly. *Taiwan. J. Obstet. Gynecol.* **60**, 840–850 (2021).
11. J. W. Oh, C. W. Park, K. C. Moon, J. S. Park, J. K. Jun, Fetal inflammatory response is positively correlated with the progress of inflammation in chorionic plate. *Placenta* **97**, 6–17 (2020).
12. K. C. Moon, J. W. Oh, C. W. Park, J. S. Park, J. K. Jun, The relationship among intra-amniotic inflammatory response, the progression of inflammation in chorionic plate and early-onset neonatal sepsis. *Front. Pediatr.* **9**, 582472 (2021).
13. V. G. Jain, K. A. Willis, A. Jobe, N. Ambalavanan, Chorioamnionitis and neonatal outcomes. *Pediatr. Res.* **91**, 289–296 (2022).
14. A. Giraud, M. J. Allard, M. Segura, F. Roche, H. Patural, G. Sebire, Ampicillin treatment increases placental interleukin-1 beta concentration and polymorphonuclear infiltration in group B *Streptococcus*-induced chorioamnionitis: A preclinical study. *Neonatology* **117**, 369–373 (2020).
15. A. Conde-Agudelo, R. Romero, E. J. Jung, A. J. Garcia Sanchez, Management of clinical chorioamnionitis: An evidence-based approach. *Am. J. Obstet. Gynecol.* **223**, 848–869 (2020).
16. B. M. Arman, N. K. Binder, N. de Alwis, T. J. Kaitu'u-Lino, N. J. Hannan, Repurposing existing drugs as a therapeutic approach for the prevention of preterm birth. *Reproduction* **165**, R9–R23 (2023).
17. M. G. Gravett, K. M. Adams, D. W. Sadowsky, A. R. Grosvenor, S. S. Witkin, M. K. Axthelm, M. J. Novy, Immunomodulators plus antibiotics delay preterm delivery after experimental intraamniotic infection in a nonhuman primate model. *Am. J. Obstet. Gynecol.* **197**, 518.e1–518.e8 (2007).
18. F. G. Smith, A. W. Wade, M. L. Lewis, W. Qi, Cyclooxygenase (COX) inhibitors and the newborn kidney. *Pharmaceuticals* **5**, 1160–1176 (2012).
19. US Food and Drug Administration, FDA recommends avoiding use of NSAIDs in pregnancy at 20 weeks or later because they can result in low amniotic fluid. FDA drug safety. *Communication* **2020**, 1–9 (2020).
20. P. Presicce, C. W. Park, P. Senthamaraikannan, S. Bhattacharyya, C. Jackson, F. Kong, C. M. Rueda, E. DeFranco, L. A. Miller, D. A. Hildeman, N. Salomonis, C. A. Chougnet, A. H. Jobe, S. G. Kallapur, IL-1 signaling mediates intrauterine inflammation and chorio-decidua neutrophil recruitment and activation. *JCI Insight* **3**, e98306 (2018).
21. A. Li, L. Zhang, J. Li, Z. Fang, S. Li, Y. Peng, M. Zhang, X. Wang, Effect of RvD1/FPR2 on inflammatory response in chorioamnionitis. *J. Cell. Mol. Med.* **24**, 13397–13407 (2020).
22. E. Y. Chang, J. Zhang, S. Sullivan, R. Newman, I. Singh, *N*-acetylcysteine attenuates the maternal and fetal proinflammatory response to intrauterine LPS injection in an animal model for preterm birth and brain injury. *J. Matern. Fetal Neonatal Med.* **24**, 732–740 (2011).
23. M. K. Paintlia, A. S. Paintlia, A. K. Singh, I. Singh, Attenuation of lipopolysaccharide-induced inflammatory response and phospholipids metabolism at the feto-maternal interface by *N*-acetyl cysteine. *Pediatr. Res.* **64**, 334–339 (2008).
24. R. Beloosesky, D. A. Gayle, M. G. Ross, Maternal *N*-acetylcysteine suppresses fetal inflammatory cytokine responses to maternal lipopolysaccharide. *Am. J. Obstet. Gynecol.* **195**, 1053–1057 (2006).
25. M. Lappas, M. Permezel, G. E. Rice, *N*-acetyl-cysteine inhibits phospholipid metabolism, proinflammatory cytokine release, protease activity, and nuclear factor-κB deoxyribonucleic acid-binding activity in human fetal membranes in vitro. *J. Clin. Endocrinol. Metab.* **88**, 1723–1729 (2003).
26. A. Y. Shahin, I. M. Hassanin, A. M. Ismail, J. S. Kruessel, J. Hirchenhain, Effect of oral *N*-acetyl cysteine on recurrent preterm labor following treatment for bacterial vaginosis. *Int. J. Gynaecol. Obstet.* **104**, 44–48 (2009).
27. J. A. Keelan, S. Khan, F. Yosaatmadja, M. D. Mitchell, Prevention of inflammatory activation of human gestational membranes in an ex vivo model using a pharmacological NF-κB inhibitor. *J. Immunol.* **183**, 5270–5278 (2009).
28. D. De Silva, M. D. Mitchell, J. A. Keelan, Inhibition of choriodecidual cytokine production and inflammatory gene expression by selective I-κB kinase (IKK) inhibitors. *Br. J. Pharmacol.* **160**, 1808–1822 (2010).
29. D. J. Ireland, M. W. Kemp, Y. Miura, M. Saito, J. P. Newnham, J. A. Keelan, Intra-amniotic pharmacological blockade of inflammatory signalling pathways in an ovine chorioamnionitis model. *Mol. Hum. Reprod.* **21**, 479–489 (2015).
30. B. S. Kaplan, I. Restaino, D. S. Raval, R. P. Gottlieb, J. Bernstein, Renal failure in the neonate associated with in utero exposure to non-steroidal anti-inflammatory agents. *Pediatr. Nephrol.* **8**, 700–704 (1994).
31. D. W. Sadowsky, G. J. Haluska, M. G. Gravett, S. S. Witkin, M. J. Novy, Indomethacin blocks interleukin 1β-induced myometrial contractions in pregnant rhesus monkeys. *Am. J. Obstet. Gynecol.* **183**, 173–180 (2000).
32. N. Yim, S. W. Ryu, K. Choi, K. R. Lee, S. Lee, H. Choi, J. Kim, M. R. Shaker, W. Sun, J. H. Park, D. Kim, W. D. Heo, C. Choi, Exosome engineering for efficient intracellular delivery of soluble proteins using optically reversible protein-protein interaction module. *Nat. Commun.* **7**, 12277 (2016).
33. C. Jobin, A. Panja, C. Hellerbrand, Y. Iimuro, J. Didonato, D. A. Brenner, R. B. Sartor, Inhibition of proinflammatory molecule production by adenovirus-mediated expression of a nuclear factor κB super-repressor in human intestinal epithelial cells. *J. Immunol.* **160**, 410–418 (1998).
34. D. J. Van Antwerp, I. M. Verma, Signal-induced degradation of IκBα: Association with NF-κB and the PEST sequence in IκBα are not required. *Mol. Cell. Biol.* **16**, 6037–6045 (1996).
35. S. Sheller-Miller, E. Radnaa, J.-K. Yoo, E. Kim, K. Choi, Y. Kim, Y. N. Kim, L. Richardson, C. Choi, R. Menon, Exosomal delivery of NF-κB inhibitor delays LPS-induced preterm birth and modulates fetal immune cell profile in mouse models. *Sci. Adv.* **7**, eabd3865 (2021).
36. H. Choi, Y. Kim, A. Mirzaaghasi, J. Heo, Y. N. Kim, J. H. Shin, S. Kim, N. H. Kim, E. S. Cho, J. I. Yook, T.-H. Yoo, E. Song, P. Kim, E.-C. Shin, K. Chung, K. Choi, C. Choi, Exosome-based delivery of super-repressor IκBα relieves sepsis-associated organ damage and mortality. *Sci. Adv.* **6**, eaaz6980 (2020).
37. S. Kim, S. A. Lee, H. Yoon, M. Y. Kim, J. K. Yoo, S. H. Ahn, C. H. Park, J. Park, B. Y. Nam, J. T. Park, S. H. Han, S. W. Kang, N. H. Kim, H. S. Kim, D. Han, J. I. Yook, C. Choi, T. H. Yoo, Exosome-based delivery of super-repressor IκBα ameliorates kidney ischemia-reperfusion injury. *Kidney Int.* **100**, 570–584 (2021).
38. J. S. Chae, H. Park, S.-H. Ahn, E.-C. Han, Y. Lee, Y. J. Kim, E.-J. Ahn, H.-W. Oh, H. J. Lee, C. Choi, Y.-H. Choi, W.-J. Kim, The effect of super-repressor IkB-loaded exosomes (Exo-srIκBs) in chronic post-ischemia pain (CPIP) models. *Pharmaceutics* **15**, 553 (2023).
39. H.-I. Lee, M.-J. Ahn, J.-K. Yoo, S.-H. Ahn, S. Y. Park, H. Seo, M.-J. Kim, Y. J. Lee, H. H. Jang, S. C. Shim, E. J. Won, C. Park, C. Choi, T.-J. Kim, Exosome-mediated delivery of super-repressor IκBα alleviates inflammation and joint damages in rheumatoid arthritis. *Arthritis Res. Ther.* **26**, 2 (2024).
40. C.-J. Lee, S. H. Jang, J. Lim, H. Park, S.-H. Ahn, S. Y. Park, H. Seo, S.-J. Song, J.-A. Shin, C. Choi, H. Y. Gee, Y.-H. Choi, Exosome-based targeted delivery of NF-κB ameliorates age-related neuroinflammation in the aged mouse brain. *Exp. Mol. Med.* **57**, 235–248 (2025).

41. A. F. Schmidt, P. S. Kannan, C. A. Chougnet, S. C. Danzer, L. A. Miller, A. H. Jobe, S. G. Kallapur, Intra-amniotic LPS causes acute neuroinflammation in preterm rhesus macaques. *J. Neuroinflammation* **13**, 238 (2016).
42. C. M. Rueda, P. Presicce, C. M. Jackson, L. A. Miller, S. G. Kallapur, A. H. Jobe, C. A. Chougnet, Lipopolysaccharide-induced chorioamnionitis promotes IL-1-dependent inflammatory $FOXP3^+$ $CD4^+$ T cells in the fetal Rhesus Macaque. *J. Immunol.* **196**, 3706–3715 (2016).
43. K. L. Wong, J. J.-Y. Tai, W.-C. Wong, H. Han, X. Sem, W.-H. Yeap, P. Kourilsky, S.-C. Wong, Gene expression profiling reveals the defining features of the classical, intermediate, and nonclassical human monocyte subsets. *Blood* **118**, e16–e31 (2011).
44. C. Weber, K. U. Belge, P. von Hundelshausen, G. Draude, B. Steppich, M. Mack, M. Frankenberger, K. S. Weber, H. W. Ziegler-Heitbrock, Differential chemokine receptor expression and function in human monocyte subpopulations. *J. Leukoc. Biol.* **67**, 699–704 (2000).
45. J. Cros, N. Cagnard, K. Woollard, N. Patey, S. Y. Zhang, B. Senechal, A. Puel, S. K. Biswas, D. Moshous, C. Picard, J. P. Jais, D. D'Cruz, J. L. Casanova, C. Trouillet, F. Geissmann, Human CD14dim monocytes patrol and sense nucleic acids and viruses via TLR7 and TLR8 receptors. *Immunity* **33**, 375–386 (2010).
46. T. D. Gilmore, Introduction to NF-κB: Players, pathways, perspectives. *Oncogene* **25**, 6680–6684 (2006).
47. O. Shynlova, T. Nedd-Roderique, Y. Li, A. Dorogin, T. Nguyen, S. J. Lye, Infiltration of myeloid cells into decidua is a critical early event in the labour cascade and post-partum uterine remodelling. *J. Cell. Mol. Med.* **17**, 311–324 (2013).
48. S. Hamilton, Y. Oomomian, G. Stephen, O. Shynlova, C. L. Tower, A. Garrod, S. J. Lye, R. L. Jones, Macrophages infiltrate the human and rat decidua during term and preterm labor: Evidence that decidual inflammation precedes labor. *Biol. Reprod.* **86**, 39 (2012).
49. K. Motomura, R. Romero, J. Galaz, L. Tao, V. Garcia-Flores, Y. Xu, B. Done, M. Arenas-Hernandez, D. Miller, P. Gutierrez-Contreras, M. Farias-Jofre, S. Aras, L. I. Grossman, A. L. Tarca, N. Gomez-Lopez, Fetal and maternal NLRP3 signaling is required for preterm labor and birth. *JCI Insight* **7**, e158238 (2022).
50. P. Presicce, P. Senthamaraikannan, M. Alvarez, C. M. Rueda, M. Cappelletti, L. A. Miller, A. H. Jobe, C. A. Chougnet, S. G. Kallapur, Neutrophil recruitment and activation in decidua with intra-amniotic IL-1beta in the preterm rhesus macaque. *Biol. Reprod.* **92**, 56 (2015).
51. R. Vento-Tormo, M. Efremova, R. A. Botting, M. Y. Turco, M. Vento-Tormo, K. B. Meyer, J. E. Park, E. Stephenson, K. Polański, A. Goncalves, L. Gardner, S. Holmqvist, J. Henriksson, A. Zou, A. M. Sharkey, B. Millar, B. Innes, L. Wood, A. Wilbrey-Clark, R. P. Payne, M. A. Ivarsson, S. Lisgo, A. Filby, D. H. Rowitch, J. N. Bulmer, G. J. Wright, M. J. T. Stubbington, M. Haniffa, A. Moffett, S. A. Teichmann, Single-cell reconstruction of the early maternal-fetal interface in humans. *Nature* **563**, 347–353 (2018).
52. F. O. Martinez, S. Gordon, M. Locati, A. Mantovani, Transcriptional profiling of the human monocyte-to-macrophage differentiation and polarization: New molecules and patterns of gene expression. *J. Immunol.* **177**, 7303–7311 (2006).
53. S. Aibar, C. B. González-Blas, T. Moerman, V. A. Huynh-Thu, H. Imrichova, G. Hulselmans, F. Rambow, J. C. Marine, P. Geurts, J. Aerts, J. van den Oord, Z. K. Atak, J. Wouters, S. Aerts, SCENIC: Single-cell regulatory network inference and clustering. *Nat. Methods* **14**, 1083–1086 (2017).
54. S. C. Sun, J. H. Chang, J. Jin, Regulation of nuclear factor-κB in autoimmunity. *Trends Immunol.* **34**, 282–289 (2013).
55. J. Han, J. D. Lee, L. Bibbs, R. J. Ulevitch, A MAP kinase targeted by endotoxin and hyperosmolarity in mammalian cells. *Science* **265**, 808–811 (1994).
56. K. Yamaoka, T. Otsuka, H. Niiro, Y. Arinobu, Y. Niho, N. Hamasaki, K. Izuhara, Activation of STAT5 by lipopolysaccharide through granulocyte-macrophage colony-stimulating factor production in human monocytes. *J. Immunol.* **160**, 838–845 (1998).
57. A. Kimura, T. Naka, T. Muta, O. Takeuchi, S. Akira, I. Kawase, T. Kishimoto, Suppressor of cytokine signaling-1 selectively inhibits LPS-induced IL-6 production by regulating JAK-STAT. *Proc. Natl. Acad. Sci. U.S.A.* **102**, 17089–17094 (2005).
58. S. Jin, C. F. Guerrero-Juarez, L. Zhang, I. Chang, R. Ramos, C. H. Kuan, P. Myung, M. V. Plikus, Q. Nie, Inference and analysis of cell-cell communication using CellChat. *Nat. Commun.* **12**, 1088 (2021).
59. P. Presicce, M. Cappelletti, P. Senthamaraikannan, F. Ma, M. Morselli, C. M. Jackson, S. Mukherjee, L. A. Miller, M. Pellegrini, A. H. Jobe, C. A. Chougnet, S. G. Kallapur, TNF-signaling modulates neutrophil-mediated immunity at the feto-maternal interface during LPS-induced intrauterine inflammation. *Front. Immunol.* **11**, 558 (2020).
60. M. Tong, J. A. Potter, G. Mor, V. M. Abrahams, Lipopolysaccharide-stimulated human fetal membranes induce neutrophil activation and release of vital neutrophil extracellular traps. *J. Immunol.* **203**, 500–510 (2019).
61. N. Lawlor, D. Nehar-Belaid, J. D. S. Grassmann, M. Stoeckius, P. Smibert, M. L. Stitzel, V. Pascual, J. Banchereau, A. Williams, D. Ucar, Single cell analysis of blood mononuclear cells stimulated through either LPS or anti-CD3 and anti-CD28. *Front. Immunol.* **12**, 636720 (2021).
62. C. M. Jackson, S. Mukherjee, A. N. Wilburn, C. Cates, I. P. Lewkowich, H. Deshmukh, W. J. Zacharias, C. A. Chougnet, Pulmonary consequences of prenatal inflammatory exposures: Clinical perspective and review of basic immunological mechanisms. *Front. Immunol.* **11**, 1285 (2020).
63. A. Toth, S. Steinmeyer, P. Kannan, J. Gray, C. M. Jackson, S. Mukherjee, M. Demmert, J. R. Sheak, D. Benson, J. Kitzmiller, J. A. Wayman, P. Presicce, C. Cates, R. Rubin, K. Chetal, Y. Du, Y. Miao, M. Gu, M. Guo, V. V. Kalinichenko, S. G. Kallapur, E. R. Miraldi, Y. Xu, D. Swarr, I. Lewkowich, N. Salomonis, L. Miller, J. S. Sucre, J. A. Whitsett, C. A. Chougnet, A. H. Jobe, H. Deshmukh, W. J. Zacharias, Inflammatory blockade prevents injury to the developing pulmonary gas exchange surface in preterm primates. *Sci. Transl. Med.* **14**, eabl8574 (2022).
64. T. Liu, L. Zhang, D. Joo, S. C. Sun, NF-κB signaling in inflammation. *Signal Transduct. Target. Ther.* **2**, 17023 (2017).
65. S. Girard, L. Tremblay, M. Lepage, G. Sébire, IL-1 receptor antagonist protects against placental and neurodevelopmental defects induced by maternal inflammation. *J. Immunol.* **184**, 3997–4005 (2010).
66. Y. Xu, R. Romero, D. Miller, L. Kadam, T. N. Mial, O. Plazyo, V. Garcia-Flores, S. S. Hassan, Z. Xu, A. L. Tarca, S. Drewlo, N. Gomez-Lopez, An M1-like macrophage polarization in decidual tissue during spontaneous preterm labor that is attenuated by rosiglitazone treatment. *J. Immunol.* **196**, 2476–2491 (2016).
67. L. Reyes, T. G. Golos, Hofbauer cells: Their role in healthy and complicated pregnancy. *Front. Immunol.* **9**, 2628 (2018).
68. M. Joerink, E. Rindsjö, B. van Riel, J. Alm, N. Papadogiannakis, Placental macrophage (Hofbauer cell) polarization is independent of maternal allergen-sensitization and presence of chorioamnionitis. *Placenta* **32**, 380–385 (2011).
69. M. T. Vinnars, E. Rindsjö, S. Ghazi, A. Sundberg, N. Papadogiannakis, The number of $CD68^+$ (Hofbauer) cells is decreased in placentas with chorioamnionitis and with advancing gestational age. *Pediatr. Dev. Pathol.* **13**, 300–304 (2010).
70. T. H. Hung, S. F. Chen, J. J. Hsu, C. C. Hsieh, S. Hsueh, T. T. Hsieh, Tumour necrosis factor-alpha converting enzyme in human gestational tissues from pregnancies complicated by chorioamnionitis. *Placenta* **27**, 996–1006 (2006).
71. P. Toti, F. Arcuri, Z. Tang, F. Schatz, E. Zambrano, G. Mor, T. Niven-Fairchild, V. M. Abrahams, G. Krikun, C. J. Lockwood, S. Guller, Focal increases of fetal macrophages in placentas from pregnancies with histological chorioamnionitis: Potential role of fibroblast monocyte chemotactic protein-1. *Am. J. Reprod. Immunol.* **65**, 470–479 (2011).
72. M. J. Kim, R. Romero, M. T. Gervasi, J. S. Kim, W. Yoo, D. C. Lee, P. Mittal, O. Erez, J. P. Kusanovic, S. S. Hassan, C. J. Kim, Widespread microbial invasion of the chorioamniotic membranes is a consequence and not a cause of intra-amniotic infection. *Lab. Invest.* **89**, 924–936 (2009).
73. EPPPIC Group, Evaluating Progestogens for Preventing Preterm birth International Collaborative (EPPPIC): Meta-analysis of individual participant data from randomised controlled trials. *Lancet* **397**, 1183–1194 (2021).
74. N. M. Shah, P. F. Lai, N. Imami, M. R. Johnson, Progesterone-related immune modulation of pregnancy and labor. *Front. Endocrinol.* **10**, 198 (2019).
75. L. Sykes, P. R. Bennett, Efficacy of progesterone for prevention of preterm birth. *Best Pract. Res. Clin. Obstet. Gynaecol.* **52**, 126–136 (2018).
76. P. Presicce, M. Cappelletti, M. Morselli, F. Ma, P. Senthamaraikannan, G. Protti, B. B. Nadel, L. Aryan, M. Eghbali, L. Salwinski, N. Pithia, E. De Franco, L. A. Miller, M. Pellegrini, A. H. Jobe, C. A. Chougnet, S. G. Kallapur, Amnion responses to intrauterine inflammation and effects of inhibition of TNF signaling in preterm Rhesus macaque. *iScience* **26**, 108118 (2023).
77. B. W. Kramer, S. G. Kallapur, T. J. Moss, I. Nitsos, G. P. Polglase, J. P. Newnham, A. H. Jobe, Modulation of fetal inflammatory response on exposure to lipopolysaccharide by chorioamnion, lung, or gut in sheep. *Am. J. Obstet. Gynecol.* **202**, 77.e1–77.e9 (2010).
78. W. M. Gilbert, T. R. Moore, R. A. Brace, Amniotic fluid volume dynamics. *Fetal Matern. Med. Rev.* **3**, 89–104 (1991).
79. H. Maeda, J. Wu, T. Sawa, Y. Matsumura, K. Hori, Tumor vascular permeability and the EPR effect in macromolecular therapeutics: A review. *J. Control. Release* **65**, 271–284 (2000).
80. R. K. Jain, Transport of molecules across tumor vasculature. *Cancer Metastasis Rev.* **6**, 559–593 (1987).
81. F. Danhier, To exploit the tumor microenvironment: Since the EPR effect fails in the clinic, what is the future of nanomedicine? *J. Control. Release* **244**, 108–121 (2016).
82. H. Choi, M. Y. Kim, D. H. Kim, H. Yun, B. K. Oh, S. B. Kim, I. H. Song, H. S. Park, S. E. Kim, C. Park, C. Choi, Quantitative biodistribution and pharmacokinetics study of GMP-grade exosomes labeled with ^{89}Zr radioisotope in mice and rats. *Pharmaceutics* **14**, 1118 (2022).
83. S. Sheller-Miller, K. Choi, C. Choi, R. Menon, Cyclic-recombinase-reporter mouse model to determine exosome communication and function during pregnancy. *Am. J. Obstet. Gynecol.* **221**, 502.e1–502.e12 (2019).
84. R. Espín-Palazón, D. Traver, The NF-κB family: Key players during embryonic development and HSC emergence. *Exp. Hematol.* **44**, 519–527 (2016).

85. T. M. Lindström, P. R. Bennett, The role of nuclear factor kappa B in human labour. *Reproduction* **130**, 569–581 (2005).
86. O. Seppänen, V. Glumoff, R. Paananen, S. Rounioja, M. Hallman, Transcription factors NF-κB and C/EBPδ and IL-1-induced expression of surfactant protein A in lung explants during the perinatal period. *Biol. Neonate* **87**, 152–159 (2005).
87. V. A. Londhe, H. T. Nguyen, J. M. Jeng, X. Li, C. Li, C. Tiozzo, N. Zhu, P. Minoo, NF-kB induces lung maturation during mouse lung morphogenesis. *Dev. Dyn.* **237**, 328–338 (2008).
88. C. K. Weber, S. Liptay, T. Wirth, G. Adler, R. M. Schmid, Suppression of NF-κB activity by sulfasalazine is mediated by direct inhibition of IκB kinases α and β. *Gastroenterology* **119**, 1209–1218 (2000).
89. M. J. Allard, A. Giraud, M. Segura, G. Sebire, Sex-specific maternofetal innate immune responses triggered by group B *Streptococci*. *Sci. Rep.* **9**, 8587 (2019).
90. C. M. Salafia, C. Weigl, L. Silberman, The prevalence and distribution of acute placental inflammation in uncomplicated term pregnancies. *Obstet. Gynecol.* **73**, 383–389 (1989).
91. A. L. Hein, M. Mukherjee, G. A. Talmon, S. K. Natarajan, T. M. Nordgren, E. Lyden, C. K. Hanson, J. L. Cox, A. Santiago-Pintado, M. A. Molani, M. Van Ormer, M. Thompson, M. Thoene, A. Akhter, A. Anderson-Berry, A. G. Yuil-Valdes, QuPath digital immunohistochemical analysis of placental tissue. *J. Pathol. Inform.* **12**, 40 (2021).
92. R. J. Porter, S. Din, P. Bankhead, A. Oniscu, M. J. Arends, QuPath algorithm accurately identifies MLH1-deficient inflammatory bowel disease-associated colorectal cancers in a tissue microarray. *Diagnostics* **13**, 1890 (2023).
93. L. Sibley, O. Daykin-Pont, C. Sarfas, J. Pascoe, A. D. White, S. Sharpe, Differences in host immune populations between rhesus macaques and cynomolgus macaque subspecies in relation to susceptibility to *Mycobacterium tuberculosis* infection. *Sci. Rep.* **11**, 8810 (2021).
94. Z. B. Bjornson-Hooper, G. K. Fragiadakis, M. H. Spitzer, H. Chen, D. Madhireddy, K. Hu, K. Lundsten, D. R. McIlwain, G. P. Nolan, A comprehensive atlas of immunological differences between humans, mice, and non-human primates. *Front. Immunol.* **13**, 867015 (2022).
95. G. Matute-Bello, G. Downey, B. B. Moore, S. D. Groshong, M. A. Matthay, A. S. Slutsky, W. M. Kuebler, Acute Lung Injury in Animals Study Group, An official American Thoracic Society workshop report: Features and measurements of experimental acute lung injury in animals. *Am. J. Respir. Cell Mol. Biol.* **44**, 725–738 (2011).
96. G. Park, S. S. Kim, J. Shim, S.-J. V. Lee, Brief guide to immunostaining. *Mol. Cells* **48**, 100157 (2025).
97. Y. Hao, S. Hao, E. Andersen-Nissen, W. M. Mauck III, S. Zheng, A. Butler, M. J. Lee, A. J. Wilk, C. Darby, M. Zager, P. Hoffman, M. Stoeckius, E. Papalexi, E. P. Mimitou, J. Jain, A. Srivastava, T. Stuart, L. M. Fleming, B. Yeung, A. J. Rogers, J. M. McElrath, C. A. Blish, R. Gottardo, P. Smibert, R. Satija, Integrated analysis of multimodal single-cell data. *Cell* **184**, 3573–3587.e29 (2021).
98. G. D. Kim, C. Lim, J. Park, A practical handbook on single-cell RNA sequencing data quality control and downstream analysis. *Mol. Cells* **47**, 100103 (2024).
99. S. Choudhary, R. Satija, Comparison and evaluation of statistical error models for scRNA-seq. *Genome Biol.* **23**, 27 (2022).
100. J. F. Deniset, P. Kubes, Neutrophil heterogeneity: Bona fide subsets or polarization states? *J. Leukoc. Biol.* **103**, 829–838 (2018).
101. R. Grieshaber-Bouyer, P. A. Nigrovic, Neutrophil heterogeneity as therapeutic opportunity in immune-mediated disease. *Front. Immunol.* **10**, 346 (2019).
102. C. Silvestre-Roig, Z. G. Fridlender, M. Glogauer, P. Scapini, Neutrophil diversity in health and disease. *Trends Immunol.* **40**, 565–583 (2019).
103. X. Xie, Q. Shi, P. Wu, X. Zhang, H. Kambara, J. Su, H. Yu, S. Y. Park, R. Guo, Q. Ren, S. Zhang, Y. Xu, L. E. Silberstein, T. Cheng, F. Ma, C. Li, H. R. Luo, Single-cell transcriptome profiling reveals neutrophil heterogeneity in homeostasis and infection. *Nat. Immunol.* **21**, 1119–1133 (2020).
104. P. Yang, Y. Li, Y. Xie, Y. Liu, Different faces for different places: Heterogeneity of neutrophil phenotype and function. *J. Immunol. Res.* **2019**, 8016254 (2019).
105. M.-C. Wagle, D. Kirouac, C. Klijn, B. Liu, S. Mahajan, M. Junttila, J. Moffat, M. Merchant, L. Huw, M. Wongchenko, K. Okrah, S. Srinivasan, Z. Mounir, T. Sumiyoshi, P. M. Haverty, R. L. Yauch, Y. Yan, O. Kabbarah, G. Hampton, L. Amler, S. Ramanujan, M. R. Lackner, S.-M. A. Huang, A transcriptional MAPK pathway activity score (MPAS) is a clinically relevant biomarker in multiple cancer types. *NPJ Precis. Oncol.* **2**, 7 (2018).
106. I. Joanito, P. Wirapati, N. Zhao, Z. Nawaz, G. Yeo, F. Lee, C. L. P. Eng, D. C. Macalinao, M. Kahraman, H. Srinivasan, V. Lakshmanan, S. Verbandt, P. Tsantoulis, N. Gunn, P. N. Venkatesh, Z. W. Poh, R. Nahar, H. L. J. Oh, J. M. Loo, S. Chia, L. F. Cheow, E. Cheruba, M. T. Wong, L. Kua, C. Chua, A. Nguyen, J. Golovan, A. Gan, W.-J. Lim, Y. A. Guo, C. K. Yap, B. Tay, Y. Hong, D. Q. Chong, A.-Y. Chok, W.-Y. Park, S. Han, M. H. Chang, I. Seow-En, C. Fu, R. Mathew, E.-L. Toh, L. Z. Hong, A. J. Skanderup, R. D. Gupta, C.-A. J. Ong, K. H. Lim, E. K. W. Tan, S.-L. Koo, W. Q. Leow, S. Tejpar, S. Prabhakar, I. B. Tan, Single-cell and bulk transcriptome sequencing identifies two epithelial tumor cell states and refines the consensus molecular classification of colorectal cancer. *Nat. Genet.* **54**, 963–975 (2022).
107. D. M. Mosser, J. P. Edwards, Exploring the full spectrum of macrophage activation. *Nat. Rev. Immunol.* **8**, 958–969 (2008).
108. Y. Yao, X. H. Xu, L. Jin, Macrophage polarization in physiological and pathological pregnancy. *Front. Immunol.* **10**, 792 (2019).
109. S. Durinck, P. T. Spellman, E. Birney, W. Huber, Mapping identifiers for the integration of genomic datasets with the R/Bioconductor package biomaRt. *Nat. Protoc.* **4**, 1184–1191 (2009).
110. J. W. Squair, M. Gautier, C. Kathe, M. A. Anderson, N. D. James, T. H. Hutson, R. Hudelle, T. Qaiser, K. J. E. Matson, Q. Barraud, A. J. Levine, G. La Manno, M. A. Skinnider, G. Courtine, Confronting false discoveries in single-cell differential expression. *Nat. Commun.* **12**, 5692 (2021).
111. K. D. Zimmerman, M. A. Espeland, C. D. Langefeld, A practical solution to pseudoreplication bias in single-cell studies. *Nat. Commun.* **12**, 738 (2021).
112. S. Junttila, J. Smolander, L. L. Elo, Benchmarking methods for detecting differential states between conditions from multi-subject single-cell RNA-seq data. *Brief. Bioinform.* **23**, bbac286 (2022).
113. M. I. Love, W. Huber, S. Anders, Moderated estimation of fold change and dispersion for RNA-seq data with DESeq2. *Genome Biol.* **15**, 550 (2014).
114. T. Wu, E. Hu, S. Xu, M. Chen, P. Guo, Z. Dai, T. Feng, L. Zhou, W. Tang, L. Zhan, X. Fu, S. Liu, X. Bo, G. Yu, clusterProfiler 4.0: A universal enrichment tool for interpreting omics data. *Innovation (Camb)* **2**, 100141 (2021).
115. J. Qu, F. Yang, T. Zhu, Y. Wang, W. Fang, Y. Ding, X. Zhao, X. Qi, Q. Xie, M. Chen, Q. Xu, Y. Xie, Y. Sun, D. Chen, A reference single-cell regulomic and transcriptomic map of cynomolgus monkeys. *Nat. Commun.* **13**, 4069 (2022).
116. S. Hänzelmann, R. Castelo, J. Guinney, GSVA: Gene set variation analysis for microarray and RNA-seq data. *BMC Bioinformatics* **14**, 7 (2013).

Acknowledgments: We would like to express gratitude to T. Kim, Y. Kim, and Y. Jeon from GE Healthcare Korea for invaluable assistance and unwavering support. In addition, we thank laboratory members for data discussion and critiquing the manuscript. **Funding:** This research was supported by a MD-Phd/Medical Scientist Training Program grant through the Korea Health Industry Development Institute (KHIDI) to S.H.J., funded by the Ministry of Health & Welfare, Republic of Korea. This work was also supported by grants from the Korea Health Technology R&D Project through the KHIDI, funded by the Ministry of Health & Welfare, Republic of Korea (grant number HI21C187101 to C.-W.P., J.-S.K., and C.C. and RS-2024000438709 to H.Y.G.). **Author contributions:** Conceptualization: H.C., S.-B.Y., C.P., J.-S.K., C.C., C.-W.P., and H.Y.G. Methodology: S.H.J., H.C., J.K.W., S.-B.Y., C.P., J.-S.K., and C.C. Resources: H.C., E.M.L., J.K.W., S.-B.Y., C.P., J.-S.K., C.C., and H.Y.G. Investigation: S.H.J., H.C., E.M.L., J.K.W., S.H.S., S.-B.Y., C.P., H.-J.K., J.-S.K., and C.-W.P. Data curation: H.C., C.P., J.-S.K., and H.Y.G. Validation: S.H.J., H.C., E.M.L., J.K.W., S.-B.Y., C.P., J.-S.K., C.C., and H.Y.G. Supervision: C.P., J.-S.K., C.C., C.-W.P., and H.Y.G. Funding acquisition: C.P., C.C., C.-W.P., and H.Y.G. Project administration: C.P., S.-B.Y., J.-S.K., C.C., C.-W.P., and H.Y.G. Formal analysis: S.H.J., H.C., J.K.W., C.P., J.-S.K., and H.Y.G. Software: S.H.J. Visualization: S.H.J., H.C., H.-J.K., J.K.W., C.P., J.-S.K., C.C., and H.Y.G. Writing—original draft: S.H.J., H.C., S.-B.Y., C.P., J.-S.K., C.C., and H.Y.G. Writing—review and editing: H.C., S.H.S., H.-J.K., C.P., J.-S.K., and C.-W.P. **Competing interests:** C.C. is the founder and shareholder, while H.C., H.-J.K., and C.P. are minor shareholders of ILIAS Biologics Inc. All other authors declare that they have no competing interests. **Data and materials availability:** The scRNA-seq and bulk RNA-seq data presented in this study have been deposited in the Korea Sequence Read Archive (KRA) of the Korea Bioinformation Center (Korea Research Institute of Bioscience and Biotechnology) under the accession number KAP230705 (https://kbds.re.kr/KRA). All data needed to evaluate the conclusions in the paper are present in the paper and/or the Supplementary Materials. Materials used in this study are available to academic researchers through a material transfer agreement with the Primate Resources Center (PRC), KRIBB, and ILIAS Biologics Inc.

Submitted 4 March 2024
Accepted 28 May 2025
Published 2 July 2025
10.1126/sciadv.adp0467